Three-Dimensional Idealized Simulations of Barrier Jets along the Southeast Coast of Alaska

JOSEPH B. OLSON* AND BRIAN A. COLLE

School of Marine and Atmospheric Sciences, Stony Brook University, Stony Brook, New York

(Manuscript received 5 December 2007, in final form 20 June 2008)

ABSTRACT

Three-dimensional idealized simulations using the fifth-generation Pennsylvania State University–NCAR Mesoscale Model (MM5) down to 6-km grid spacing were performed in order to understand how different ambient conditions (wind speed and direction, stability, and inland cold pool) and terrain characteristics impact barrier jets along the southeastern Alaskan coast. The broad inland terrain of western North America is important in Alaskan jet development, since it rotates the impinging flow cyclonically (more coast parallel) well upstream of the coast, thus favoring more low-level flow blocking while also adding momentum and width to the barrier jet. Near the steep coastal terrain, the largest wind speed enhancement factor (1.9–2.0) in the terrain-parallel direction relative to the ambient onshore-directed wind speed occurs at relatively low Froude numbers (Fr $\sim$ 0.3–0.4). These low Froude numbers are associated with (10–15 m s^{-1}) ambient wind speeds and wind directions orientated 30°–45° from terrain-parallel. For simulations with an inland cold pool and nearly coast-parallel flow, strong gap outflows develop through the coastal mountain gaps, shifting the largest wind speed enhancement to Fr $<$ 0.2. The widest barrier jets occur with ambient winds oriented nearly terrain-parallel with strong static stability. The gap outflows shift the position of the jet maximum farther offshore from the coast and increase the jet width. The height of the jet maxima is typically located at the top of the shallow gap outflow ($\sim$500 m MSL), but without strong gap outflows, the jet heights are located at the top of the boundary layer, which is higher (lower) for large (small) frictionally induced vertical wind shear and weak (strong) static stability.

1. Introduction

The low-level flow from the Pacific Ocean interacts with the steep coastal terrain of Alaska to create strong ($>$25 m s^{-1}) terrain-parallel winds (Overland and Bond 1995; Loescher et al. 2006; Colle et al. 2006; Olson et al. 2007; among others) known as barrier jets (Schwerdtfeger 1974; Overland and Bond 1993, 1995). These jets can result in enhanced turbulence (Smedman et al. 1995; Bond and Walter 2002) and wind stress forcing of local currents and storm surges (Orr et al. 2005). Barrier jets often create hazardous conditions for mariners and pilots, which can result in significant losses in the fishing, shipping, and aviation industries (Macklin et al. 1990).

a. Previous observational studies of Alaskan barrier jets

Loescher et al. (2006) completed a climatology of Alaskan coastal barrier jets and noted both "classical" barrier jets, fed primarily by onshore flow, and "hybrid" barrier jets, which had some gap outflows at the coast. The strongest jets were located immediately adjacent to and downstream of the Fairweather and Valdez-Cordova coastal mountains, with enhanced wind speeds typically 2–3 times larger than the ambient flow. The width of most jets extended 40–60 km from the coast, but some jet widths extended as much as $\sim$250 km. Some hybrid jets were detached 10–15 km from the coast, while others had sharp wind speed boundaries (shock jets), which does not conform to the gradual offshore weakening of barrier jets observed in other studies (Parish 1982).

Olson et al. (2007, hereafter OL07) detailed the

* Current affiliation: National Research Council, and Global Systems Division, NOAA/Earth System Research Laboratory, Boulder, Colorado.

Corresponding author address: Dr. Brian A. Colle, School of Marine and Atmospheric Sciences, Stony Brook University, Stony Brook, NY 11746-5000.
E-mail: brian.colle@stonybrook.edu

DOI: 10.1175/2008MWR2480.1

© 2009 American Meteorological Society

structure and dynamics of a classical and hybrid jet sampled during the Southern Alaskan Regional Jets Experiment (SARJET; Winstead et al. 2006). The classical jet had maximum winds >30 m s^{-1} at the coast between 600 and 800 m above mean sea level (MSL) and an offshore extent of ~60 km, whereas the hybrid jet of ~30 m s^{-1} was displaced 30–40 km offshore at 500 m above MSL (OL07, their Figs. 6 and 12). For both cases, the barrier jet reached its maximum strength as the winds became more southerly, which is ~40° from coast-parallel. This suggests that the ambient wind direction has a significant influence on the evolution of the coastal jets.

b. Background theory on wide-mountain barrier jets

The barrier jets along the west coast of North America are associated with steep coastal terrain and broad inland terrain associated with the Rocky Mountain plateau. Smith (1979a,b) showed that the far upstream (>1000 km) response of a broad mountain is a combination of column stretching and lifted parcel expansion. As a column of air approaches a barrier, it undergoes vertical stretching due to the upward displacement of the isentropes aloft (Buzzi and Tibaldi 1977, their Fig. 3; Smith 1979a,b). This acts to create an upstream cyclonic turning of the impinging flow to a more barrier-parallel component.

Braun et al. (1999a) explored the impact of a two-dimensional plateau barrier, similar in width to the western United States, on barrier jets. They showed that the upstream deceleration is determined by the shortwave characteristics of the orography (mountain height, h_m, and half-width, L_m), while the barrier jet strength is related to the longwave characteristics (plateau width, L_{plat}). The upstream deceleration occurs on short time scales ($\tau \sim f^{-1}$ s), while the total barrier jet strength depends on the time scale necessary for the flow to traverse the plateau ($\tau \sim L_{\mathrm{plat}}/U_n$), which can be ~24 h (10 m s^{-1} flow over 1000-km plateau). One goal of our study is to expand the work of Braun et al. (1999a) to three dimensions in order to determine whether a particular cross-barrier flow magnitude well upstream (U_n) of the topography yields a similar barrier jet structure as the wind direction is varied.

c. Previous idealized studies using realistic terrain

Idealized studies of coastal flows using real terrain have been performed over the orography of California (Cui et al. 1998), Norway (Barstad and Grønås 2005), Taiwan (Yeh and Chen 2003), and the Alps (Zängl 2005). For example, Cui et al. (1998) varied the ambient wind direction at 45° increments for wind speeds of 7 m s^{-1} over the coastal mountains of California. They found the strongest winds occurred for wind directions oriented ~45° from terrain parallel, producing winds ~2.5 times the background wind speed. Barstad and Grønås (2005) also found that barrier jets over Norway were slightly stronger for southwesterly flows (30°–40° from parallel to the highest terrain).

d. Motivation

Given the complex orography of southern Alaska, with its inland plateau, steep coastal terrain, and many prominent coastal gaps, it needs to be determined how barrier jets evolve for different ambient wind directions and stabilities for this region. Also, previous idealized modeling studies that quantified the broad inland mountain impacts along the west coast were limited to two-dimensions and simplified terrain geometries (Braun et al. 1999a). Some questions that this study addresses are as follows:

- How does the structure of the barrier jets along the southeastern Alaskan coast depend on the ambient wind speed, wind direction, stability, and terrain variability?
- How does the gap outflow impact the structure (width, height, and strength) of the coastal jets?
- What is the contribution to the structure of the coastal jet from the broad inland plateau versus the steep coastal terrain?

The next section discusses the model configuration and methods for measuring the barrier jet properties. Section 3 compares selected idealized simulations to the case study simulations in OL07 to validate the idealized modeling approach. Section 4 addresses the large-scale response generated by the inland plateau. Sections 5 and 6 present the results for the classical and hybrid barrier jet simulations, respectively. Section 7 discusses the major findings.

2. Methodology

A set of three-dimensional idealized dry barotropic simulations on an f plane (58°N) was constructed over the Gulf of Alaska using the fifth-generation Pennsylvania State University–National Center for Atmospheric Research (NCAR) Mesoscale Model (MM5, version 3.7; Grell et al. 1995). The three computational domains had horizontal grid spacings of 54, 18, and 6 km (Fig. 1a) and were run using a one-way nest communication. The 54-km domain was large enough (>10 000 km wide), such that the fixed lateral boundary conditions did not impact the inner-nest barrier jet solutions. The model domains were modified for idealized simulations by setting the map factors to unity and

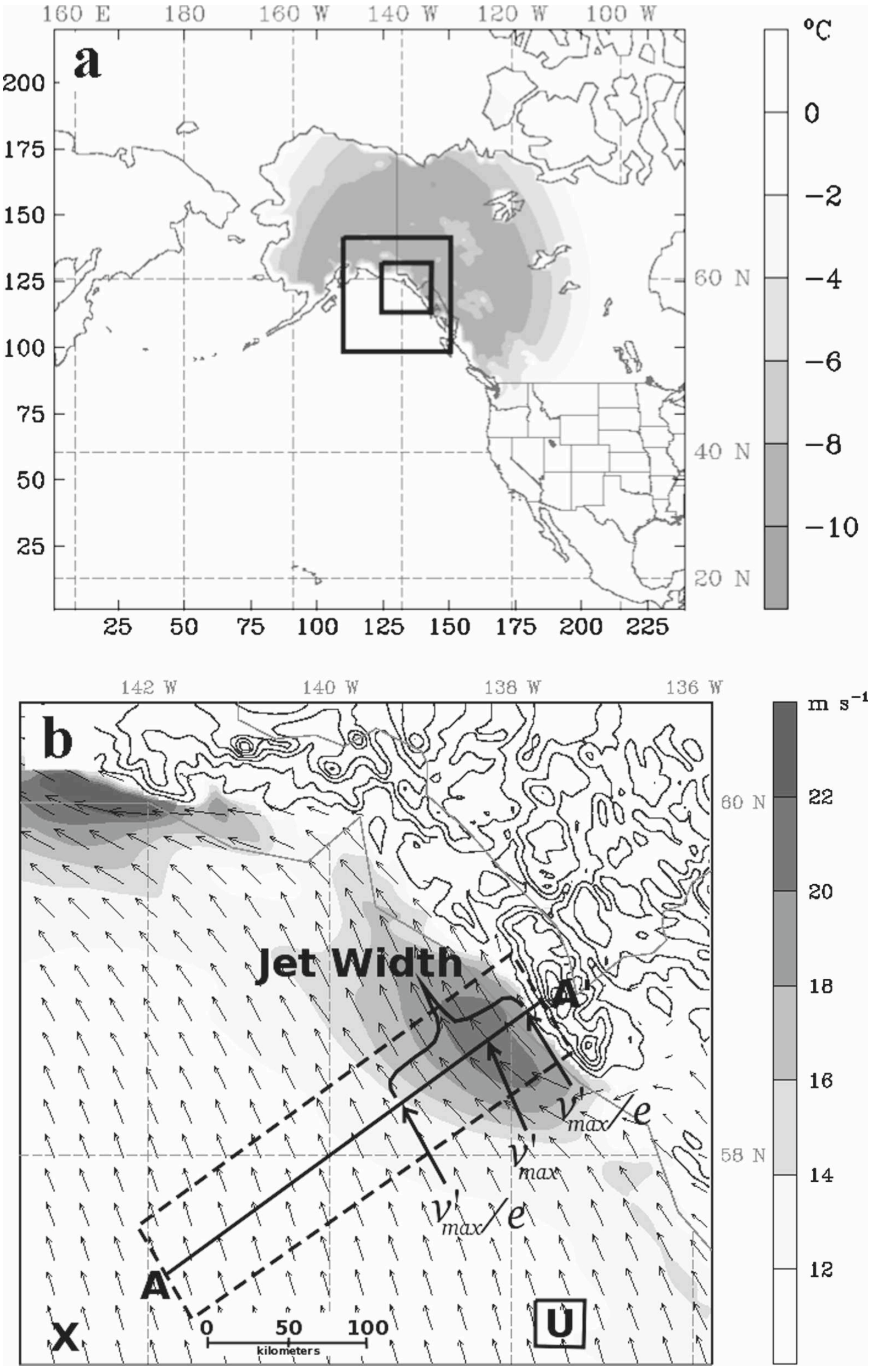

FIG. 1. (a) The 54-km domain with the 18- and 6-km nests. The 500-m-level temperature perturbation field is shown for an initialized cold pool run (gray-shaded every 2°C) with a maximum perturbation of $\Delta T = -10$°C within 1000 km of 59°N, 138°W, and decreasing linearly to zero at a 2000-km radius. (b) The 6-km nest with cross-sectional volume between A–A′. The region in box U is where a set of ambient flow conditions is measured, and its location depends on the ambient wind direction. Point X is used to measure the conditions ~500-km offshore.

TABLE 1. The set of idealized simulations used in this study, which represents a total of 104 runs (56 classical jets and 48 hybrid jets). The first two columns show the initialized wind speeds and wind directions, while the third column lists the static stabilities. The initialized strength of the inland cold pools using a fixed stability of $N = 0.01\ s^{-1}$ is shown in the fourth column.

Wind speed ($m\ s^{-1}$)	Wind direction (°)	Static stability (s^{-1})	Cold pool ($-\Delta$°C)
10	160	0.015, 0.01, 0.005	−5, −10, −15
10	180	0.015, 0.01, 0.005	−5, −10, −15
10	200	0.015, 0.01, 0.005	−5, −10, −15
10	220	0.015, 0.01, 0.005	−5, −10, −15
15	160	0.015, 0.0125, 0.01, 0.0075, 0.005	−5, −10, −15
15	180	0.015, 0.0125, 0.01, 0.0075, 0.005	−5, −10, −15
15	200	0.015, 0.0125, 0.01, 0.0075, 0.005	−5, −10, −15
15	220	0.015, 0.0125, 0.01, 0.0075, 0.005	−5, −10, −15
20	160	0.015, 0.01, 0.005	−5, −10, −15
20	180	0.015, 0.01, 0.005	−5, −10, −15
20	200	0.015, 0.01, 0.005	−5, −10, −15
20	220	0.015, 0.01, 0.005	−5, −10, −15
25	160	0.015, 0.01, 0.005	−5, −10, −15
25	180	0.015, 0.01, 0.005	−5, −10, −15
25	200	0.015, 0.01, 0.005	−5, −10, −15
25	220	0.015, 0.01, 0.005	−5, −10, −15

by removing the curvature terms from the momentum equations (Zängl 2003). Thirty-two vertical terrain-following sigma levels were used, with 14 levels below 700 hPa and a model top at 100 hPa. A 10- and 5-min land-use and topography dataset was utilized in the 54- and 18-km domains, respectively, while the 6-km domain used a 2-min terrain dataset.

The model configuration included the Blackadar planetary boundary layer (PBL; Zhang and Anthes 1982) scheme to parameterize the frictional and turbulent processes. The Blackadar scheme uses a surface roughness length over the ocean following Delsol et al. (1971). All land surface values were configured as either water or coniferous forest. The surface fluxes of heat and moisture were turned off. All runs were dry, with no convective, microphysical, or radiative parameterizations. Horizontal diffusion was calculated on height surfaces to help preserve vertical potential temperature gradients in mountainous regions (Zängl 2002). Klemp and Durran's (1983) upper-radiative boundary condition was used in order to prevent gravity waves from being reflected off the model top.

The initial and boundary conditions for the 54-km domain were created with the MM5 initialization approach described in Olson and Colle (2007). Although the scheme was originally designed for initializing a baroclinic wave, it can also specify barotropic basic states without a wave perturbation. All simulations were initialized with gradient wind-balanced barotropic flow, constant stratification in the troposphere, and a tropopause at 8.5 km MSL. A barotropic approach was used in order to better understand the terrain perturbations in the absence of thermal advections in a baroclinic system. For the hybrid jet runs an inland cold pool was initialized over the land grid points within a 1000-km radius of 59°N, 138°W (Fig. 1a), and the cold pool linearly decreased to zero at a 2000-km radius. The cold pool had temperature perturbation magnitudes of −5, −10, and −15°C below 1 km and decreased linearly to zero at 2 km MSL, which represents the depth and strength (~−8°C) of the cold anomaly in the sounding composites of hybrid jets at Whitehorse, Yukon Territory (Colle et al. 2006).

Table 1 lists the simulations used for this study. The ambient wind speeds were incremented every 5 $m\ s^{-1}$ from 10 to 25 $m\ s^{-1}$ and the wind direction every 20° from 160° to 220°, which corresponds to ~25° to 85° from coast-parallel. The static stability was incremented every 0.005 s^{-1} from $N = 0.005$ to 0.015 s^{-1}. All simulations were started impulsively and run out 48 h. Since the flow features during the early simulation period may be dependent on the startup procedure (Smolarkiewicz and Rotunno 1989), only hours 12–48 were used in the analysis. Although the real atmosphere at this latitude is more baroclinic and variable than these idealized runs, our approach represents an upper bound to a steady-state solution that can occur if a broad uniform onshore-directed flow is orientated toward the west coast with minimal temperature advections. Persistent onshore flow and weak temperature advections for more than 12 h have been observed for several case studies of terrain-forced flows in this region (Colle and Mass 1996; OL07).

Characteristic barrier jet properties, such as width, height, and wind speed enhancement, were measured for each simulation adjacent to the Fairweather Mountains (Fig. 1b), which is the same study area for OL07 and the SARJET experiment (Winstead et al. 2006).

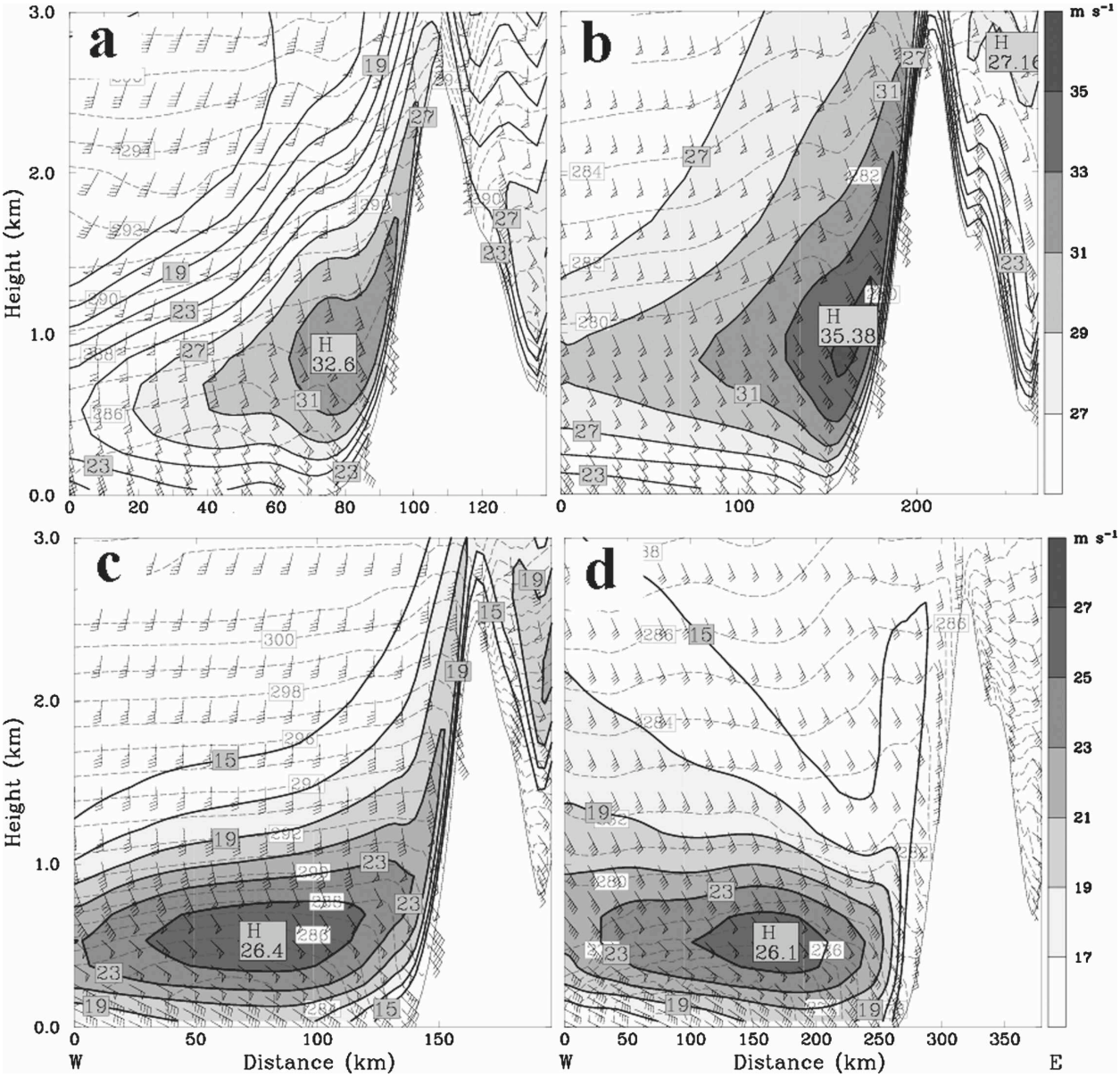

FIG. 2. Terrain-parallel wind speed (gray shaded every 2 m s^{-1}), potential temperature (dashed gray every 1 K), and wind barbs (1 flag = 25 m s^{-1} and full barb = 5 m s^{-1}) along the cross section A–A′ (Fig. 1) for (a) SARJET IOP1 and the (b) idealized simulation initialized with 25 m s^{-1} winds at 180°, and $N = 0.01$ s^{-1}. (c), (d) The same fields, but compare (c) SARJET IOP7 and the (d) idealized simulation initialized with 15 m s^{-1} winds at 160°, with $N = 0.01$ s^{-1} and a cold pool anomaly of 15°C.

These properties were measured within the cross-sectional volume A–A′ (dashed area in Fig. 1b), which extends 100 km along the coast, ~400 km offshore, and includes the lowest 14 sigma levels (~2.7 km MSL). This volume is taller than the mean mountain height (~2500 m), but shorter than the tallest peak (Mt. Fairweather ~3200 m) in the model terrain. The barrier-parallel wind speed was first averaged along NW–SE sections within box around A–A′ in Fig. 1b in order to obtain mean cross-barrier profiles of the jets. Barrier jet characteristics were then determined from this averaged A–A′ cross section.

The barrier jet width is defined as the horizontal distance between the outer (southwestern) and inner (northeastern) edge of the jet. The jet edges are located by first calculating the maximum terrain-parallel wind speed perturbation ($v' = v - V_0$, where v is the time-varying barrier-parallel wind speed and V_0 is the initialized barrier-parallel wind speed) between the surface and the mean mountain height for each point along

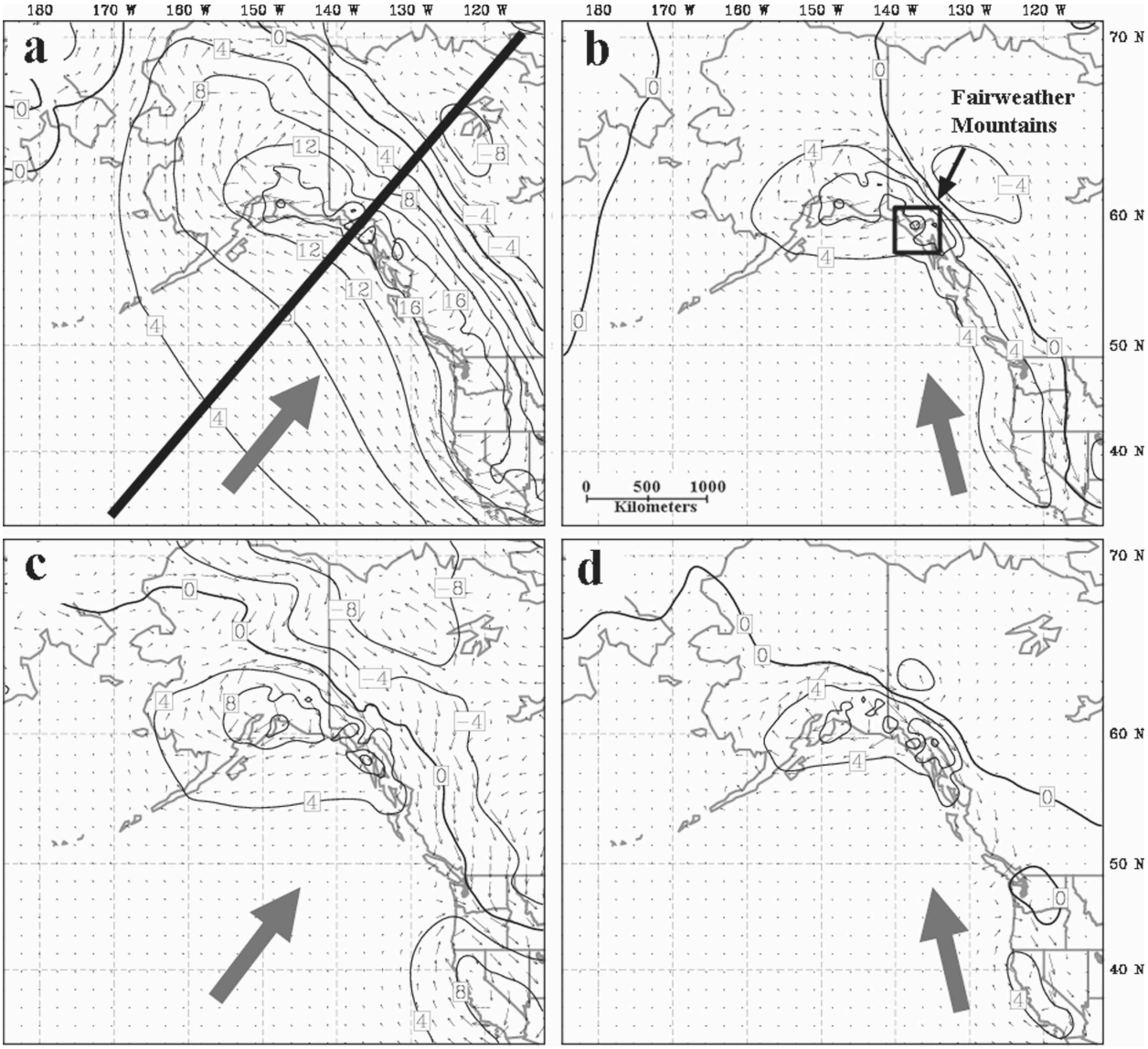

FIG. 3. Pressure (black every 4 mb) and wind perturbation at 1 km MSL at hour 24 for simulations initialized with 10 m s^{-1} and $N = 0.01$ s^{-1} for wind directions of (a) 220°, (b) 160°, (c) 220° NIT, and (d) 160° NIT. The dark gray arrows show the initialized wind direction.

the averaged A–A′ cross section. Then the jet edges are located where the maximum v' decreases by a factor of e^{-1} to both sides of the jet maximum (Fig. 1b).[1] When the inner (eastern) edge of the jet is located over the slope of the barrier, the base of the windward slope is taken as the position of the inner edge of the jet. The barrier jet height is the height of the maximum terrain-parallel wind speed in cross-section A–A′. To compare results with previous theoretical studies of barrier jets (Pierrehumbert and Wyman 1985; Braun et al. 1999a,b), the wind speed enhancement is defined as the maximum barrier-parallel wind speed perturbation (v') in A–A′ divided by U_n, the ambient barrier-normal wind speed.[2] For this study, the Froude number is defined as a time-dependent quantity:

[1] The barrier-parallel component was used as opposed to the total wind speed to be consistent with the barrier-parallel jet definition used in Loescher et al. (2006).

[2] The U_n in this study is the time-dependent mean barrier-normal component (at the base of the southeastern slope of the Fairweathers) between the surface and 2.5 km MSL at ~2000 km offshore in the 54-km domain, which avoids the influence of the broad inland terrain while including the frictional Ekman layer impact on the flow.

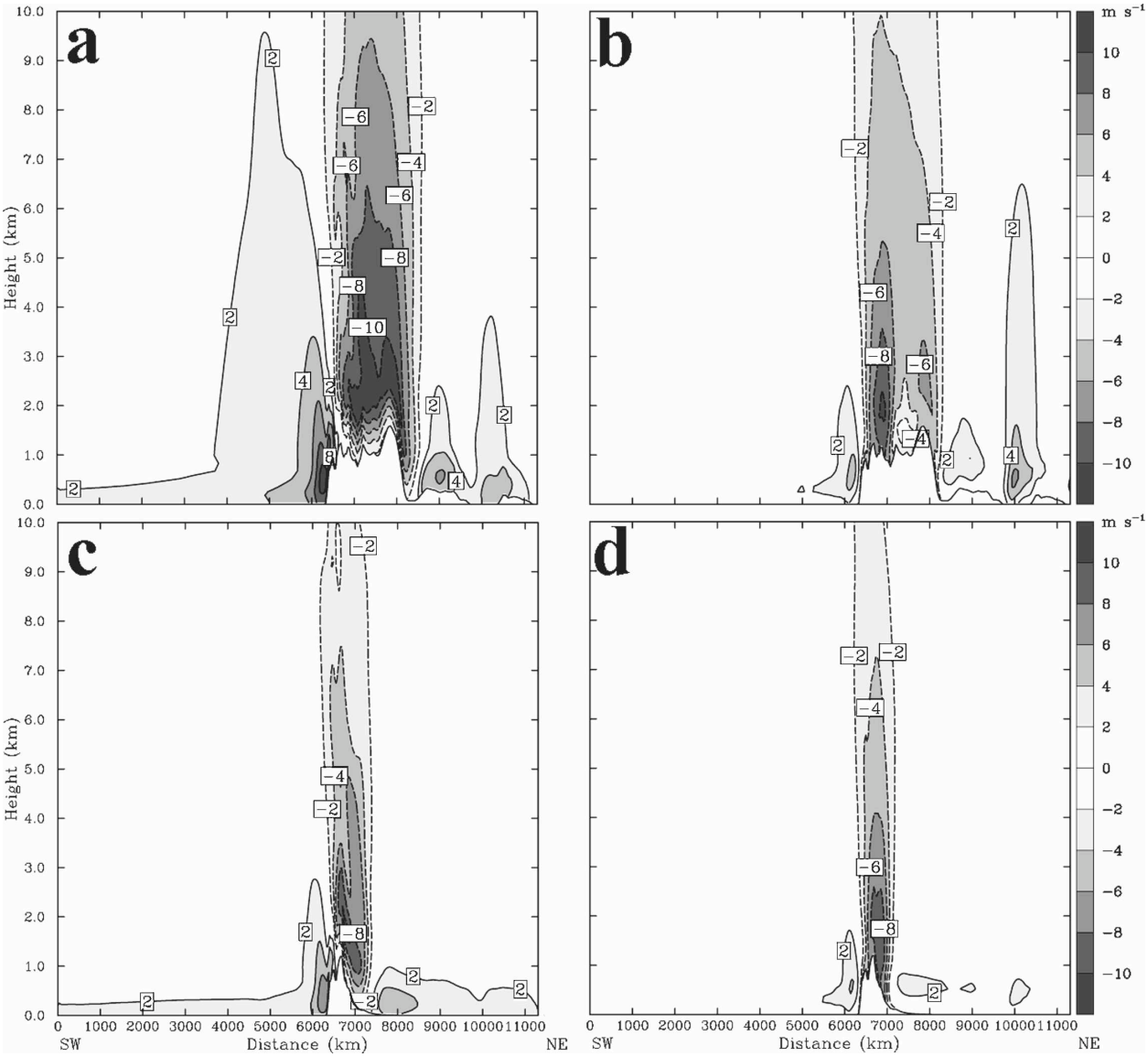

FIG. 4. Cross-sectional averages of the coast-parallel wind speed perturbation (gray-shaded every 2 m s^{-1}) within ±100 km normal to the cross section in Fig. 3a for the wind directions of (a) 220°, (b) 160°, (c) 220° NIT, and (d) 160° NIT.

$$\mathrm{Fr}(t) = \frac{1}{h}\frac{\sum_{k=1}^{k_{\max}} U_n(t,k)}{\sum_{k=1}^{k_{\max}} N(t,k)}, \qquad (1)$$

since U_n and N evolve as the boundary layer develops. Therefore a bulk quantity through a depth h (~2.5 km) is averaged over the lowest $k_{\max}$ (=14) model levels.

Previous case studies of Alaskan barrier jets related jet properties (enhancement, width, and height) to upstream conditions a few hundred kilometers upstream of the barrier (Loescher et al. 2006; OL07). Therefore, the properties of the simulated jets in our study are sometimes plotted as a function of the immediate upstream conditions within the box U (Fig. 1b). This upstream box was positioned according to the ambient wind direction, such that a forward trajectory released from box U at 500 m MSL would approach the southwestern slopes of the Fairweather Mountains.

3. Comparison with SARJET case studies

To show the capability of our idealized simulations to predict realistic coastal flows even for simplified physics

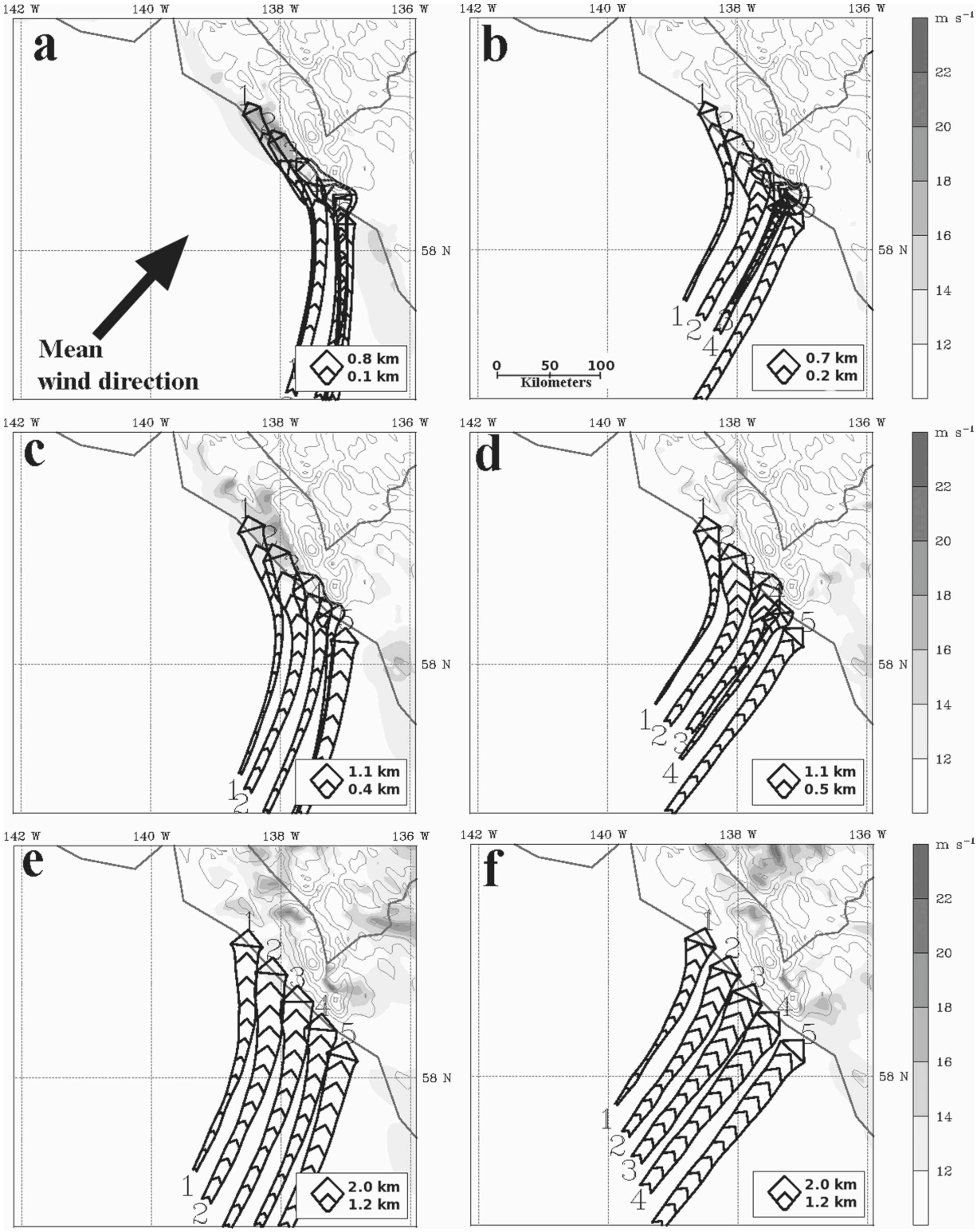

FIG. 5. Backward trajectories released over the coast at hour 24 for simulations with (left) the full topography and (right) NIT. The vertical levels for trajectory release are (a), (b) 500 m MSL; (c), (d) 1000 m MSL; and (e), (f) 2000 m MSL. The simulations were initialized with wind speeds of 10 m s^{-1}, 220°, and $N = 0.01\ s^{-1}$. The width of the arrow indicates the height above mean sea level. The total wind speed is shaded (every 2 m s^{-1}).

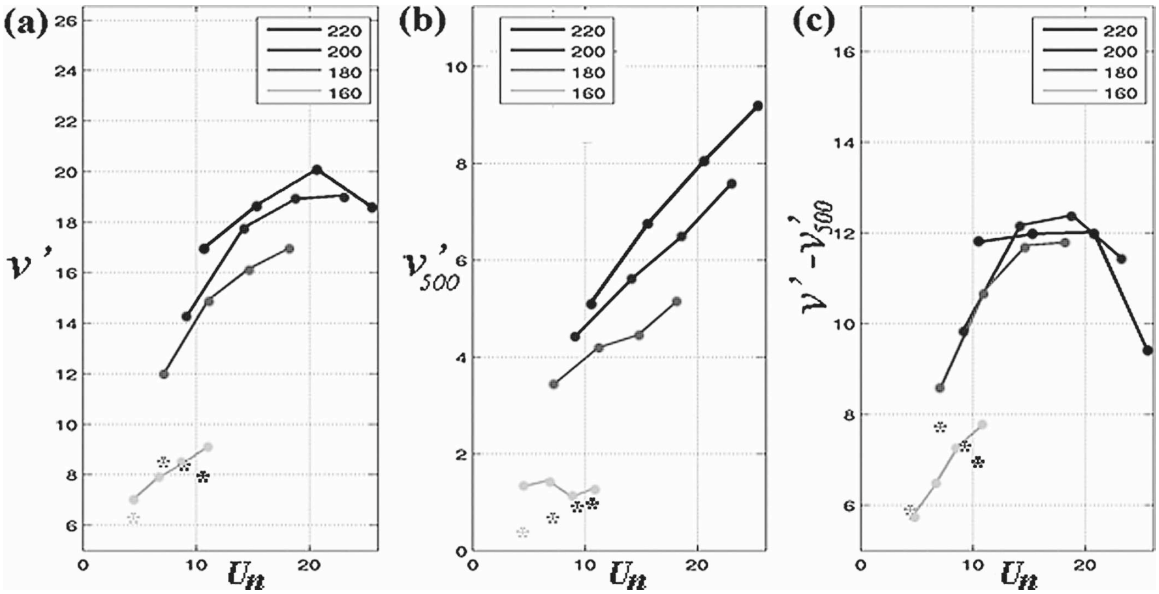

FIG. 6. (a) Maximum barrier-parallel velocity, v', within the A–A′ box in Fig. 1b as a function of U_n for different initialized wind directions (gray-shaded lines), (b) v' associated with the mountain anticyclone (measured at upstream point X in Fig. 1b), and (c) the difference between (a) and (b), which yields the v' generated within the coastal zone (<500 km offshore). The NIT runs are plotted as asterisks and are gray shaded, the same as the full terrain runs.

in the MM5, two idealized simulations were completed using ambient conditions similar to that measured ~300 km offshore in SARJET 4-km MM5 simulations of OL07. Hour 12 of the idealized runs was used to compare with the SARJET events, since the ambient flow in the case studies persisted for ~12 h before surface trough passage.

Using the ambient conditions in OL07 for intensive observing period 1 (IOP1; 2000 UTC 26 September 2004) (see their Fig. 4), an idealized simulation consisting of ambient southerly (180°) winds of 25 m s^{-1} and a dry N = 0.01 s^{-1} (RH was ~90%) were used to compare with IOP1. A vertical cross section along A–A′ (Figs. 2a,b) shows the terrain-parallel wind speeds and potential temperatures through the barrier jet for the SARJET IOP1 and idealized runs. The jet is ~1 m s^{-1} stronger in the idealized case and it is ~20–50 km wider than the IOP1 jet above 1 km MSL, since the approaching trough reduced the offshore extent of the IOP1 jet above midmountain level. The development of the well-mixed boundary layer and ~100-m higher placement of the jet maximum in the idealized simulation was likely due to a neglect of surface fluxes, which can maintain stratification in prefrontal boundary layers (Bond and Fleagle 1988). The horizontal structure of the jet around the Fairweathers was also realistically simulated using the idealized approach (Olson 2007). IOP7 (2200 UTC 12 October 2004 in OL07) featured gap outflow southwest of the Fairweathers, with southeasterly flow of ~15 m s^{-1} farther offshore to the southwest (Fig. 8 of OL07). An idealized simulation was initialized using ambient southeast (160°) winds at 15 m s^{-1}, N = 0.01 s^{-1}, and an inland cold pool with a magnitude of −15°C up to 1000 m MSL (not shown). The maximum winds at 500 m MSL in the SARJET IOP and the idealized simulations are ~26 m s^{-1} southwest of the Fairweathers at ~50 km offshore (Figs. 2c,d). The coldest temperatures are also situated ~50 km offshore as a result of the gap outflow (Figs. 2c,d). Overall, the wind speed enhancement, jet height, and width were realistically simulated despite the lack of full physics in the model.

4. Impact of broad inland terrain

The complex terrain of southeast Alaska involves a broad component (e.g., the width of the inland plateau) that forces a rotationally dominated (Rossby wave) component and a short-wave component (e.g., the Fairweathers) that produces a gravity wave response. To understand how the broad inland terrain impacts the coastal flows as a function of ambient wind direction, the large-scale pressure and wind perturbations were examined within the outer 54-km grid (with no inland cold pool initialized). Figure 3 shows the 24-h pressure perturbation at 1 km above MSL for simulations initialized using a background wind speed of 10 m s^{-1}, N = 0.01 s^{-1}, and wind directions of 220° and 160°

(Figs. 3a,b). A 16–18-mb pressure perturbation develops along the windward edge of the Alaskan–Canadian coastal region for the 220° simulation, while an 8–12-mb perturbation occurs for the 160° simulation. This pressure difference results from the greater cross-barrier flow (U_n) in the 220° simulation, which results in greater upslope (adiabatic) cooling and more robust mountain (gravity) waves tilting the isentropes upward more over the coast (not shown).

Buzzi and Tibaldi (1977) and Bannon (1986) highlighted that the depth of the terrain flow response, as given by the Rossby penetration depth (NL/f, where L is the barrier width), and its upstream extent increases with the width of the mountain. Furthermore, Smith (1979b) and Bannon and Chu (1988) showed that the magnitude of the upstream-flow deflection is proportional to the cross-sectional area of the terrain. To directly show the dependence of the flow response to the barrier width, the same simulations were performed with no inland terrain (NIT) specified >500 km east of the West Coast of North America. Near the Fairweathers (Fig. 3c), the pressure perturbation for the 220° NIT run is about half as large as the 220° control run. The terrain-parallel wind speed perturbation decays more rapidly upstream of the coast in the NIT run than in the 220° control (Figs. 4a,c). Meanwhile, the pressure perturbation (6–10 mb) in the 160° NIT run is only ~30% less than the full terrain (160° control) run (Fig. 3d), since the downstream barrier width was not as largely affected by removing the inland terrain.

Backward trajectories released from the coast at 500, 1000, and 2000 m MSL starting at hour 24 for the 220° wind direction with and without the inland terrain illustrate the impact of the inland terrain on the upstream flow (Fig. 5). In agreement with linear theory (Pierrehumbert 1984; Braun et al. 1999a), which emphasizes the mountain height and slope for upstream blocking, trajectories at 500 m MSL in both simulations result in blocked flow (Figs. 5a,b). Also, the flow ascends over this blocked flow ~150 km upstream of the coast for trajectories at 1000–2000 m above MSL (Figs. 5c–f). Meanwhile, the initial 220° flow at 500 m MSL becomes more southerly in the control (full terrain) run at ~300 km upstream (southwest) of the barrier (Fig. 5a). In contrast, the trajectories approaching the coast in the NIT run are nearly orthogonal to the barrier and there is less total wind speed enhancement (Fig. 5b). Therefore, the broad mountain cyclonically turned the flow in a direction that adds momentum to the terrain-parallel barrier jet, and this flow can further accelerate down the along-barrier pressure gradient near the coast to create wind speeds exceeding 20 m s^{-1} (Fig. 5a). At 2000 m MSL (Figs. 5e,f), little blocking is evident in the

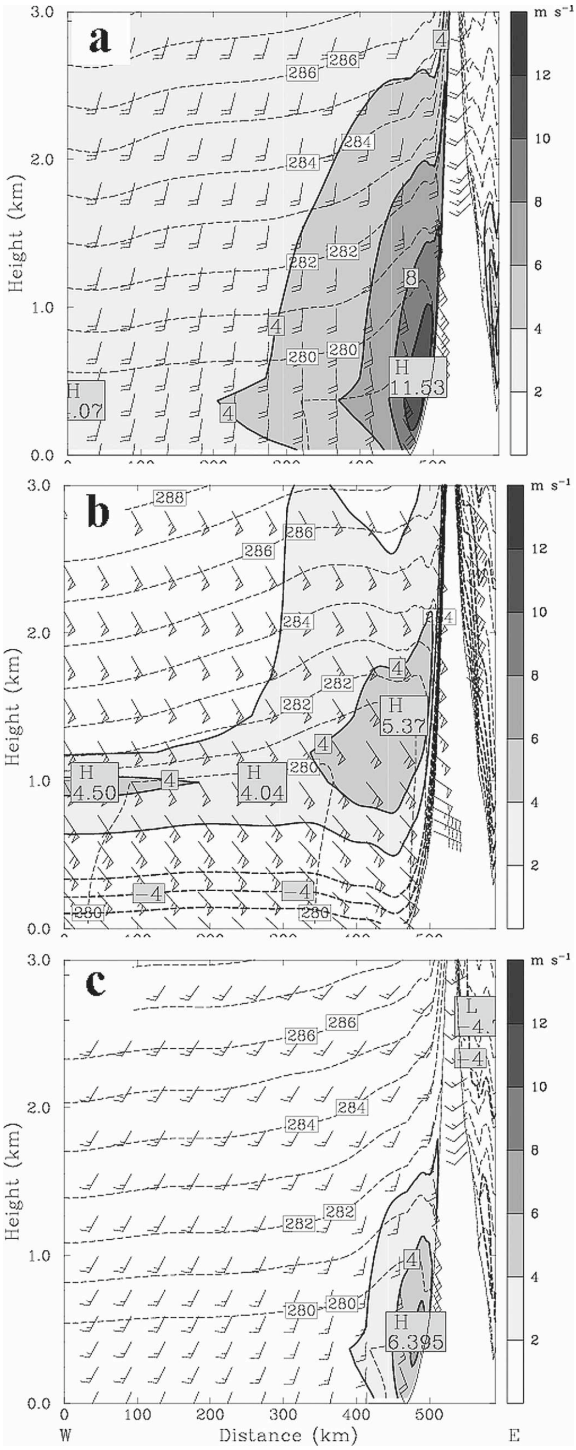

FIG. 7. The impact of wind direction and broad inland terrain along cross section A–A′ for three simulations with the same initialized U_n of 10 m s^{-1} and initialized (a) wind speeds of 10 m s^{-1} at 220° with the full terrain, (b) wind speeds of 25 m s^{-1} at 160° with the full terrain, and (c) wind speeds of 10 m s^{-1} at 220° with NIT. The perturbation barrier-parallel velocities (m s^{-1}; gray-shaded), potential temperature (every 1 K, gray contours), and wind barbs are plotted.

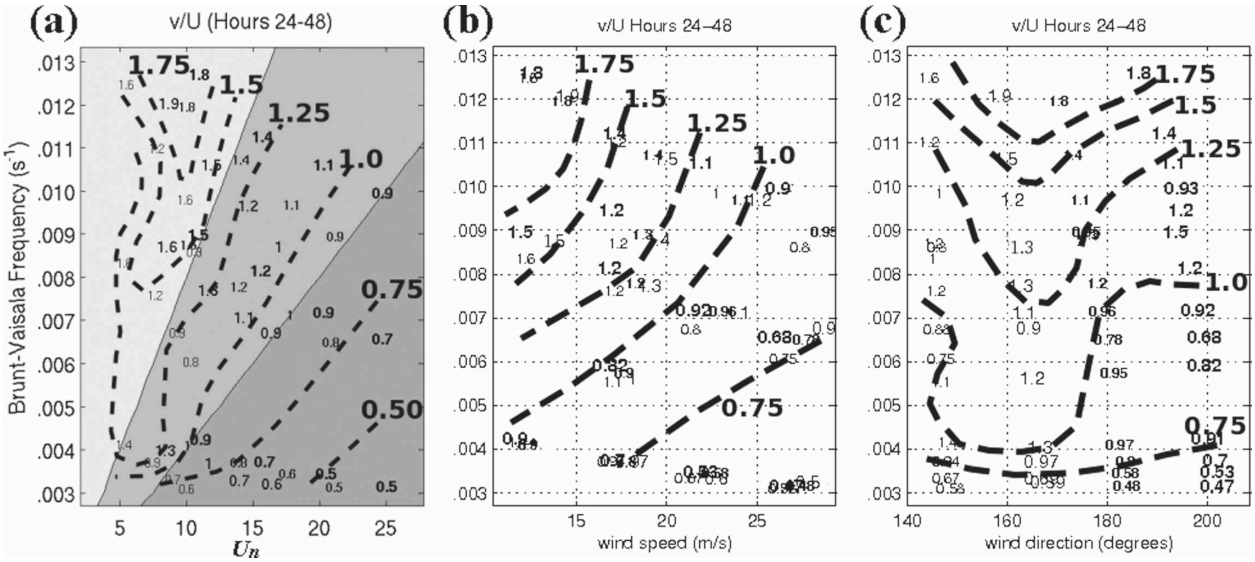

FIG. 8. Relationship between wind speed enhancement (v'/U_n, numbers and dashed, where U_n is measured at ~2000 km upstream of the barrier) for the classic jets as a function of N and (a) U_n, (b) wind speed (m s^{-1}), and (c) wind direction (°) obtained within box U (cf. Fig. 1b). The gray shades in (a) represent Froude number regimes: $0 < \mathrm{Fr} < 0.5$ (light gray), $0.5 < \mathrm{Fr} < 1.0$ (medium gray), and $1.0 < \mathrm{Fr}$ (dark gray). The different font sizes and thickness represent: 220° (large bold), 200° (small bold), 180° (large thin), and 160° (small thin). All measurements represent averages of hours 24–48.

NIT run (Fig. 5f) as compared to the control run. This suggests that the stronger mountain anticyclone for the wider terrain helps reduce the cross-barrier flow magnitude, which in turn lowers the Froude number. For example, parcels at 2000 m above MSL approaching the remaining 1200 m of Mt. Fairweather ($h_m \sim 1200$ m; $N \sim 0.01$ s^{-1}) have a lower Froude number in the control (Fr ~ 0.7) than the NIT run (Fr ~ 0.85), thus favoring more blocking in the control simulation when using the conditions a few hundred kilometers upstream of the coast ($U_n \sim 8.5$ m s^{-1} and ~ 10 m s^{-1}, respectively).

The influence of wind direction on the barrier-parallel wind speed perturbation (v') is shown as a function of the barrier-normal velocity U_n measured ~2000 km upstream of the coast (Fig. 6). Figure 6a shows the maximum v' within the A–A′ box region in Fig. 1b for the full terrain runs, which combine the near-coast accelerations and the mountain anticyclone. For the same $U_n \sim 10$ m s^{-1}, there is a ~8 m s^{-1} difference in the magnitude of v' for the various wind directions, with the largest wind perturbation associated with the more barrier-normal wind direction (220°). The v' at a point 500 km offshore (point X in Fig. 1b) is also largest for the 220° simulation (Fig. 6b), due to the development of the mountain anticyclone. The difference between the v' within A–A′ and the v' at point X represents the additional barrier-parallel acceleration closer to the coast. This difference is small for all wind directions for a given U_n (Fig. 6c), except for when the ambient flow is oriented parallel to the coast. The NIT runs with initialized wind speeds of 10 m s^{-1} for the various wind directions are also included for comparison (see * symbols in Fig. 6). The v' response for the NIT runs are similar to each other (7–9 m s^{-1}), which further highlights the importance of the inland terrain on enhancing the barrier-parallel v' by changing the large-scale flow perturbation.

Figure 7 shows a cross section of v' for flows initialized with the same $U_n = 10$ m s^{-1} but different wind directions (10 m s^{-1} at 220° and 25 m s^{-1} at 160°) at hour 24. The 160° simulation produces a 1-km pressure perturbation that is ~6 mb less than the 220° run over the Fairweathers (not shown) due to a reduction in the cross-barrier flow and mountain anticyclone. This results in a maximum terrain-parallel wind perturbation in the 160° simulation that is only half as large (Fig. 7b) compared to the 220° simulation (Fig. 7a). To show the effect of a reduced barrier width more explicitly, Fig. 7c shows the simulation with the same ambient conditions as in Fig. 7a, but with no inland terrain. The barrier jet in the NIT (220°) run is both weaker and narrower than the full-terrain 220° simulation (Figs. 7a,c).

The above analysis indicates that the "ambient flow" within box U, which is typically measured only a few hundred kilometers offshore of the coast (Overland and Bond 1995; Braun et al. 1997; Colle et al. 2002; OL07; among others), may not really represent the flow unperturbed by terrain. Rather, the broad in-

TABLE 2. Linear correlations of atmospheric parameters and the barrier jet characteristics are listed for the 56 classical barrier jet simulations for hours 24–48. There were 43 simulations with Fr < 1 and 13 with Fr > 1. The boldface values represent correlations with p values < 0.05, testing the hypothesis of no correlation against the alternative that there is a nonzero correlation.

Classical jet characteristic	Atmospheric parameter	All simulations	Fr < 1	Fr > 1
Wind speed enhancement	Barrier-normal flow	**−0.54**	**−0.38**	−0.33
	Wind speed	**−0.66**	**−0.61**	−0.52
	Wind direction	−0.26	−0.08	−0.14
	Stability	**0.75**	**0.58**	0.51
Jet width	Barrier-normal flow	**−0.58**	**−0.55**	−0.10
	Wind speed	−0.11	0.06	0.47
	Wind direction	**−0.75**	**−0.81**	−0.39
	Stability	**0.56**	**0.37**	0.15
Jet height	Wind speed	**0.75**	**0.87**	0.36
	Stability	**−0.34**	**−0.31**	−0.30

land terrain helps turns the flow more terrain parallel, which increases the strength of the jet and the potential for flow blocking against the steep coastal terrain.

5. Classical barrier jet simulations

Since the barrier jet strength and height slowly evolve after hour 24 (not shown), an average of hours 24–48 is used to diagnose the jet properties as a function of the ambient conditions. The terrain-parallel wind speed enhancement (v'/U_n), jet width, and height were related to the ambient wind speed, direction, stability, and Froude number obtained a few hundred kilometers upstream of the coast[3] (box U in Fig. 1b). This location was chosen since it represents the "ambient" flow typically measured in case studies (OL07; Loescher et al. 2006).

a. Wind speed enhancement

Figure 8a illustrates that the largest wind speed enhancements (~1.9) are associated with Fr ~ 0.3–0.4, which is consistent with flow blocking at low Froude numbers (Pierrehumbert and Wyman 1985). The barrier-normal velocity component, U_n, and the total wind

[3] Except U_n, which was obtained ~2000 km upstream of the coast as mentioned in section 2.

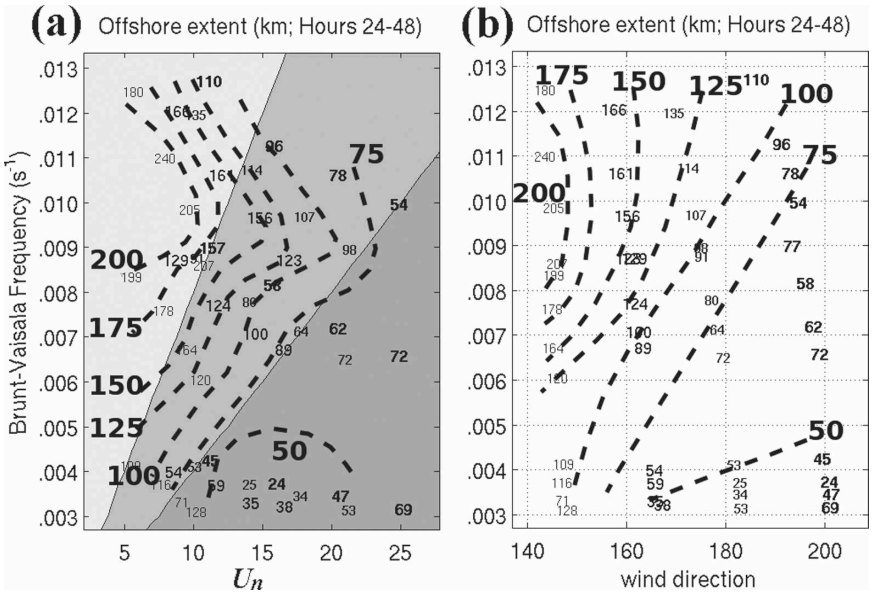

FIG. 9. Relationship between barrier jet width (numbers in km and dashed every 25 km) for the classic jets as a function of Brunt–Väisälä frequency (N) and (a) U_n and (b) wind direction. The gray shading in (a) represents Froude number regimes: 0 < Fr < 0.5 (light gray), 0.5 < Fr < 1.0 (medium gray), and 1.0 < Fr (dark gray). The variations in the size and thickness of the numbers are relative to the initialized wind direction (see Fig. 8).

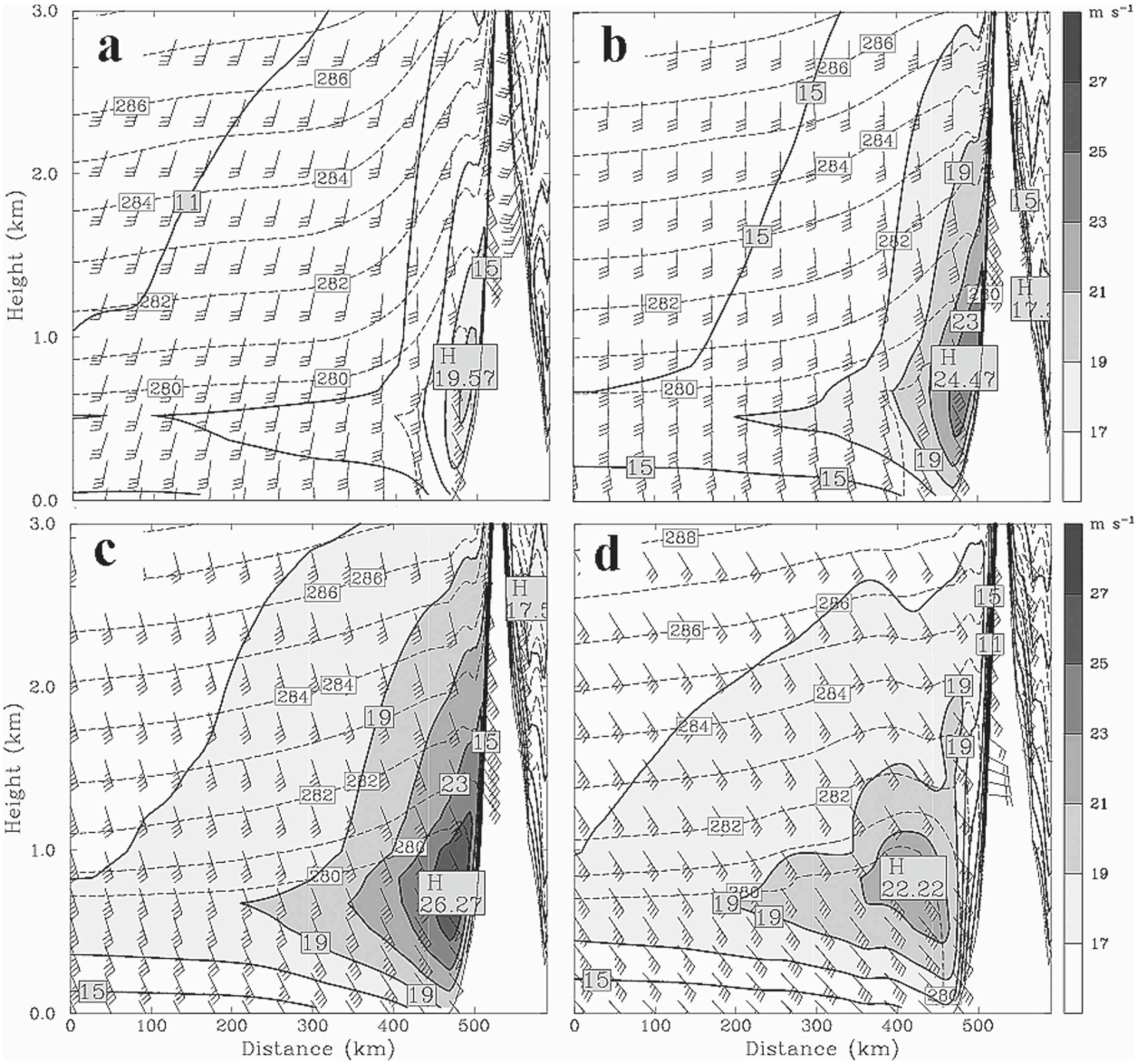

FIG. 10. Cross sections of along-barrier wind speed (gray-shaded ever 2 m s^{-1}), wind barbs (full barb = 10 kt), and potential temperature (dashed gray every 1 K) for the classic jet simulations with initialized wind speed of 15 m s^{-1}, N = 0.01 s^{-1}, and wind directions of (a) 220°, (b) 200°, (c) 180°, and (d) 160°.

speed, U_{total}, are both negatively correlated (−0.54 and −0.66, respectively, in Table 2) with the wind speed enhancement, while N has a positive correlation of 0.75. This suggests that wind speed enhancement approximately scales as Nh_m/U_n or somewhat better as Nh_m/U_{total}, given that wind speed enhancement continues to increase as the total wind speed decreases (Fig. 8b), since the flow is more easily blocked and subsequently accelerated along the coast. However, as U_n falls below ~7 m s^{-1} (Fig. 8a), the mountain-induced pressure perturbations are small, resulting in weaker accelerations. Figure 8c supports this argument by showing that the largest barrier-parallel wind speed enhancements are associated with a wind direction of ~170° (~30° from coast-parallel), since the southerly flow produces a well-defined mountain anticyclone and along-barrier pressure perturbations near the coast (not shown).[4]

[4] If Figs. 8b,c are plotted against the initialized wind speeds and wind directions (not shown), the maximum wind speed enhancement is still found for weak initialized wind speeds, but the optimal wind direction becomes centered around ~190° rather than 170° given the influence of the mountain anticyclone and Ekman layer in cyclonically turning the large-scale flow by about ~20°.

This result agrees with Petersen et al. (2003), who showed that the strongest barrier winds for wind directions oriented 30°–45° from the axis of an isolated ridge.

b. Barrier jet width

Figure 9 compares the barrier jet width with the U_n (measured >2000 km upstream), stability, and Froude number measured in box U (Fig. 9a), as well as the wind direction (Fig. 9b). Both U_n and wind direction are negatively correlated with the offshore extent of the jet (−0.56 to −0.75 in Table 2), meaning that more coast-parallel flow favors the widest jets. This negative correlation implies that an increase in U_n favors a decrease in jet width even for Fr < 1. This result is in contrast to previous studies (i.e., Overland and Bond 1995), which found that jet width was proportional to the cross-barrier wind speed ($L = U_n/f$) for Fr < 1. One possible reason for this discrepancy is that our idealized results apply to near-equilibrium solutions (hours 24–28), whereas the flow perturbation (jet) width does increase initially (hours 0–6) for increasing U_n (not shown), and may also occur for an evolving case study.

The influence of wind direction on the jet width is illustrated in Fig. 10. As an initialized wind of 15 m s^{-1} is rotated from 220° to 180° for $N \sim 0.01$ s^{-1}, the jet width increases from ~50 to ~250 km and the jet maximum moves farther offshore (Figs. 10a–c). For a wind at 180° (Fig. 10c), the coast-parallel wind speed is a combination of the large-scale mountain anticyclone superimposed on the down-gradient acceleration of southeasterly flow near the coast. Also, the Fr at box U decreases from ~0.6 to ~0.4 as the wind direction shifts from 220° to 180°, which favors more blocking and a more pronounced jet. As the wind direction is further rotated to 160° (Fig. 10d), there is little cross-barrier flow and a weak pressure perturbation near the coast (not shown), resulting in a weaker flow maximum within the broad jet. Thus, the *e*-folding definition of the barrier jet width results in widest jets for flows initialized nearly coast-parallel.

c. Barrier jet height

The height of the barrier jet maximum is most strongly correlated with the total wind speed (0.74) and stability (−0.34) measured in box U (Table 2). This suggests that the jet height scales as U_{total}/N, with low jet heights (<400 m MSL) occurring for weak wind speeds and large stabilities (Fig. 11). Over the windward slope, weaker (upslope) flow and stronger stability limits the vertical extent of the terrain-induced flow, but the offshore portion of the barrier jet in our idealized simulations are found at the top of the boundary layer, consistent with the idealized studies of Braun et al. (1999b) and Peng et al. (2001). The depth of the boundary layer is driven in part by turbulent mixing, which will be greater as the wind speed increases and/or stability decreases. The influence of wind speed on the height of the jet is shown in simulations initialized with the same stability ($N = 0.01$ s^{-1}) and wind at 180°, but the wind speeds are increased every 5 m s^{-1} from 10 to 25 m s^{-1} (Fig. 12). The jet maximum is lowest (~500 m MSL) for the 10 m s^{-1} simulation (Fig. 12a). The jet maximum rises and shifts over the windward slope when the speed is increased to 15 and 20 m s^{-1} (Figs. 12b,c). A further increase to 25 m s^{-1} lifts the jet maximum to ~1200 m MSL (Fig. 12d).

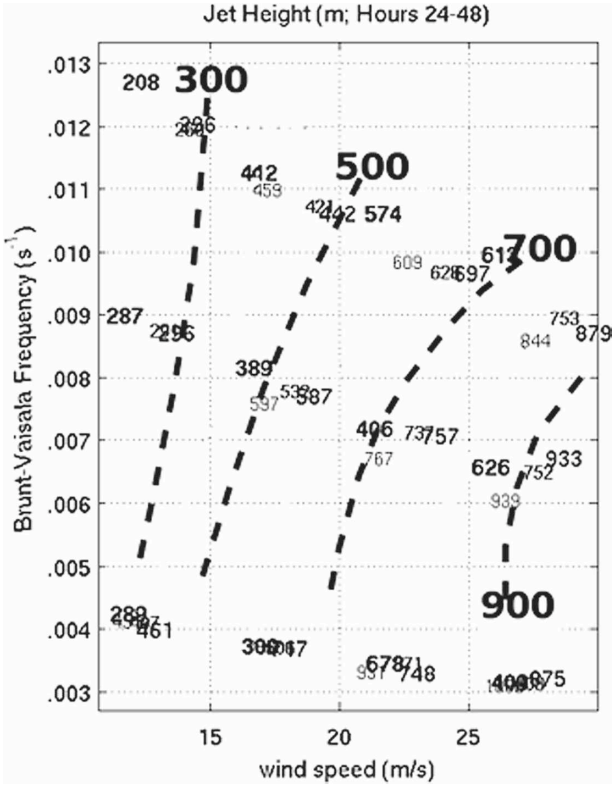

FIG. 11. Classic barrier jet height as a function of Brunt–Väisälä frequency and wind speed (m s^{-1}). The variations in the size and thickness of the numbers are relative to the initialized wind direction (see Fig. 8).

6. Hybrid barrier jet simulations

The hybrid barrier jet simulations were initialized with a constant static stability ($N = 0.01$ s^{-1}) and a 1000-m-deep cold pool over the interior varying in magnitude from $\Delta T = -5°$ to −15°C (columns 1, 2, and 4 of Table 1). A range of Fr numbers from 0.2 to 1.0 were sampled within box U in Fig. 1b, but this Fr range in-

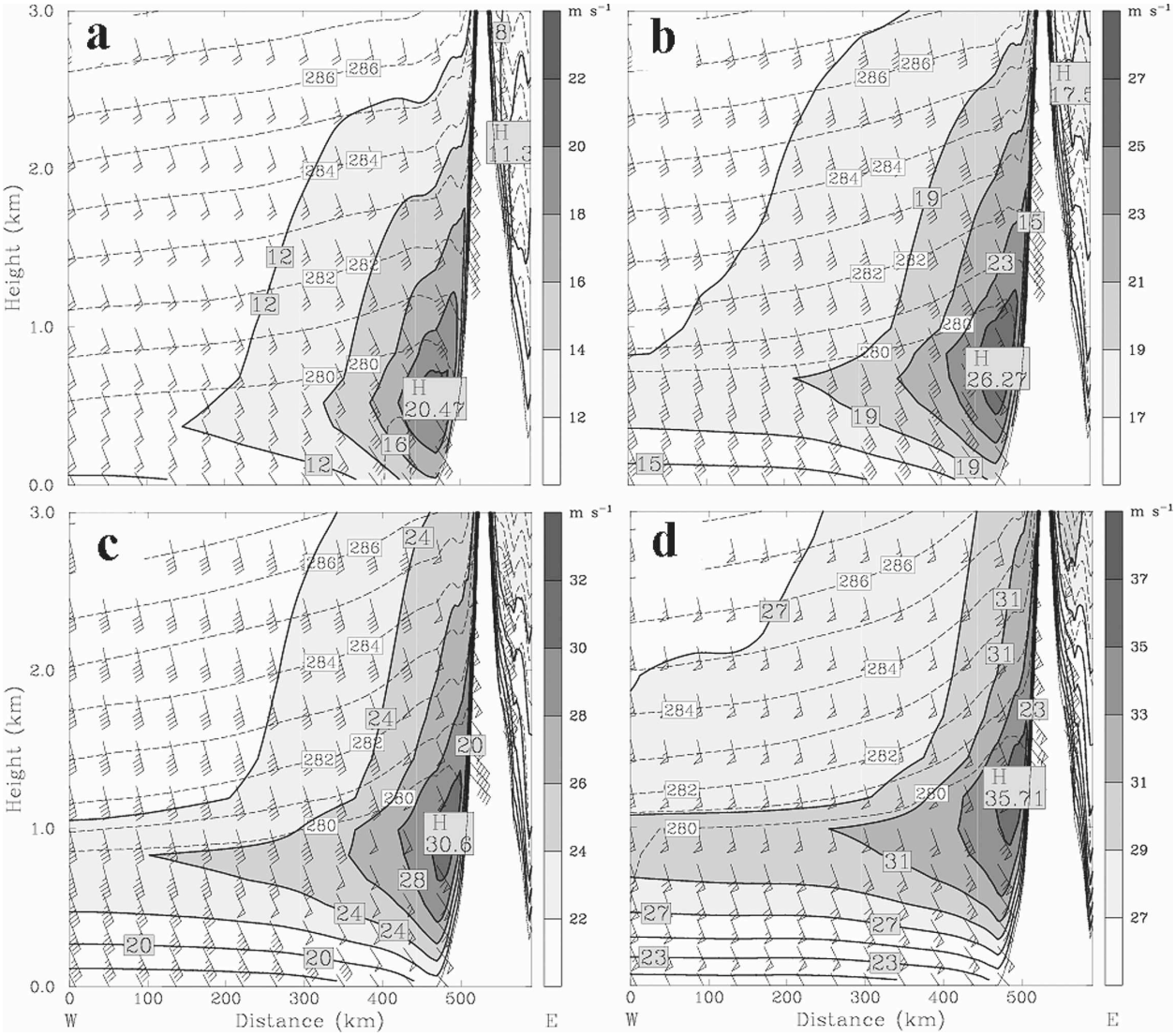

FIG. 12. Cross sections of terrain-parallel wind speed (gray shaded every 2 m s^{-1}), wind barbs (full barb = 10 kt), and potential temperature (dashed gray every 1 K) for the classic jet simulations with an initialized wind direction of 180° and static stability of N = 0.01 s^{-1} and wind speeds of (a) 10, (b) 15, (c) 20, and (d) 25 m s^{-1}.

creased during the simulations to 0.2–3.0 after the boundary layer and gap outflows developed. The stability for these simulations was measured in the 250–750 m MSL layer directly southwest of the Fairweathers, which encompasses the transition layer over the top of the gap outflow (Lackmann and Overland 1989; Overland and Bond 1995). Since the influence of the gap outflow on the hybrid jet is weak after the inland cold pool drains after hour 24, hours 12–24 are used for the analysis below.

a. Wind speed enhancement

Figure 13 shows the relationships between wind speed enhancement (v'/U_n) and U_n (measured >2000 km upstream of the coast) (Fig. 13a), wind speed (Fig. 13b), and wind direction (Fig. 13c) obtained in box U. The greatest wind speed enhancement is associated with weak (<15 m s^{-1}) ambient flows (Fig. 13b) and barrier-parallel wind direction of ~140° (Fig. 13c). In contrast to the classical jet simulations, the wind speed enhancement maximum for hybrid jets is shifted to lower Fr (<0.2) (Fig. 13a). Thus, the addition of gap outflows initiated under low Fr conditions results in large wind speed enhancements. The onshore flow component, U_n, has a slightly stronger correlation with wind speed enhancement (−0.86) than wind speed (−0.76) (Table 3), suggesting that wind speed enhancement scales slightly better with Nh_m/U_n

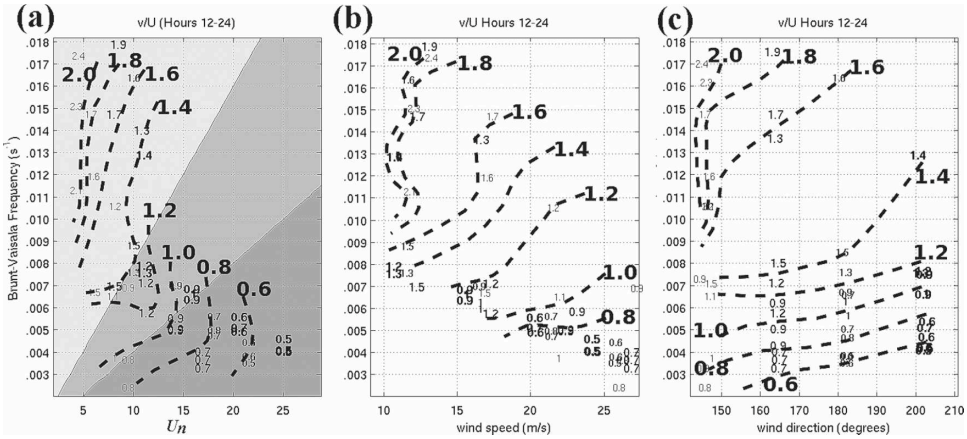

FIG. 13. Wind speed enhancement for the hybrid jets as a function of Brunt–Väisälä frequency (s^{-1}) and (a) U_n, (b) wind speed (m s^{-1}), and (c) wind direction (°). The variations in the size and thickness of the numbers are relative to the initialized wind direction (see Fig. 8) and the gray shade in (a) denotes different Fr regimes (see Fig. 8).

than Nh_m/U_{total}, which was not the case for the classical jets.

The cold pool strength has little influence on jet wind speed enhancement for simulations with ambient wind directions initialized between 180° and 220°, since the ambient pressure gradient is not oriented to effectively accelerate the cold pool through the coastal gap. However, strong gap outflows can produce strong coastal flows for the most coast-parallel flows (~160°). This acts to shift the maximum wind speed enhancements to Fr ~ 0, which is in contrast to the maximum found at Fr ~ 0.3–0.4 for the classical jets.

The relative contribution of wind speed and direction for the hybrid jets was explored at 500 m MSL (Fig. 14). The largest wind speed enhancement (~2.4) occurs for relatively weak background flow (10–15 m s^{-1}) and the most coast-parallel wind directions (160°–180°). The cases with the largest offshore-directed pressure gradient generate the largest gap outflows (top row of Fig. 14), producing the strongest winds relative to the background flow. With strong background winds (cf. upper left- and right-hand corners of Fig. 14), the gap outflow is more efficiently mixed away, resulting in a smaller impact by the gap outflow.

The terrain-parallel wind speed for cross section A–A′ also highlights the influence of wind direction on hybrid jet structure (Fig. 15). Enhanced wind speeds (>4 m s^{-1} greater than the ambient wind speed) extend more than 200 km offshore for wind directions ≤180° and the gap outflow acts to shift the position of the jet maximum ~50 km offshore (cf. the 10 m s^{-1} at 180° in Fig. 15 with the classical jet simulation in Fig. 12a). The enhancement region is reduced to <100 km offshore for more onshore-directed flow (bottom row of Fig. 15),

TABLE 3. Linear correlations of atmospheric parameters with barrier jet characteristics for the 48 hybrid barrier jet simulations for hours 12–24. There were 28 simulations with Fr < 1 and 20 with Fr > 1. The bold values represent correlations with p values < 0.05, testing the hypothesis of no correlation against the alternative that there is a nonzero correlation.

Hybrid jet characteristic	Atmospheric parameter	All simulations	Fr < 1	Fr > 1
Wind speed enhancement	Barrier-normal flow	**−0.86**	**−0.81**	**−0.86**
	Wind speed	**−0.76**	**−0.50**	**−0.55**
	Wind direction	**−0.48**	**−0.47**	**−0.72**
	Cold pool strength	0.08	0.11	−0.20
Jet width	Barrier-normal flow	**−0.77**	**−0.88**	**−0.66**
	Wind speed	−0.15	−0.12	0.35
	Wind direction	**−0.78**	**−0.89**	**−0.71**
	Cold pool strength	0.15	**0.44**	−0.18
Jet height	Wind speed	**0.81**	**0.97**	**0.65**
	Wind direction	**−0.54**	**−0.61**	**−0.75**
	Cold pool strength	0.02	0.15	0.08

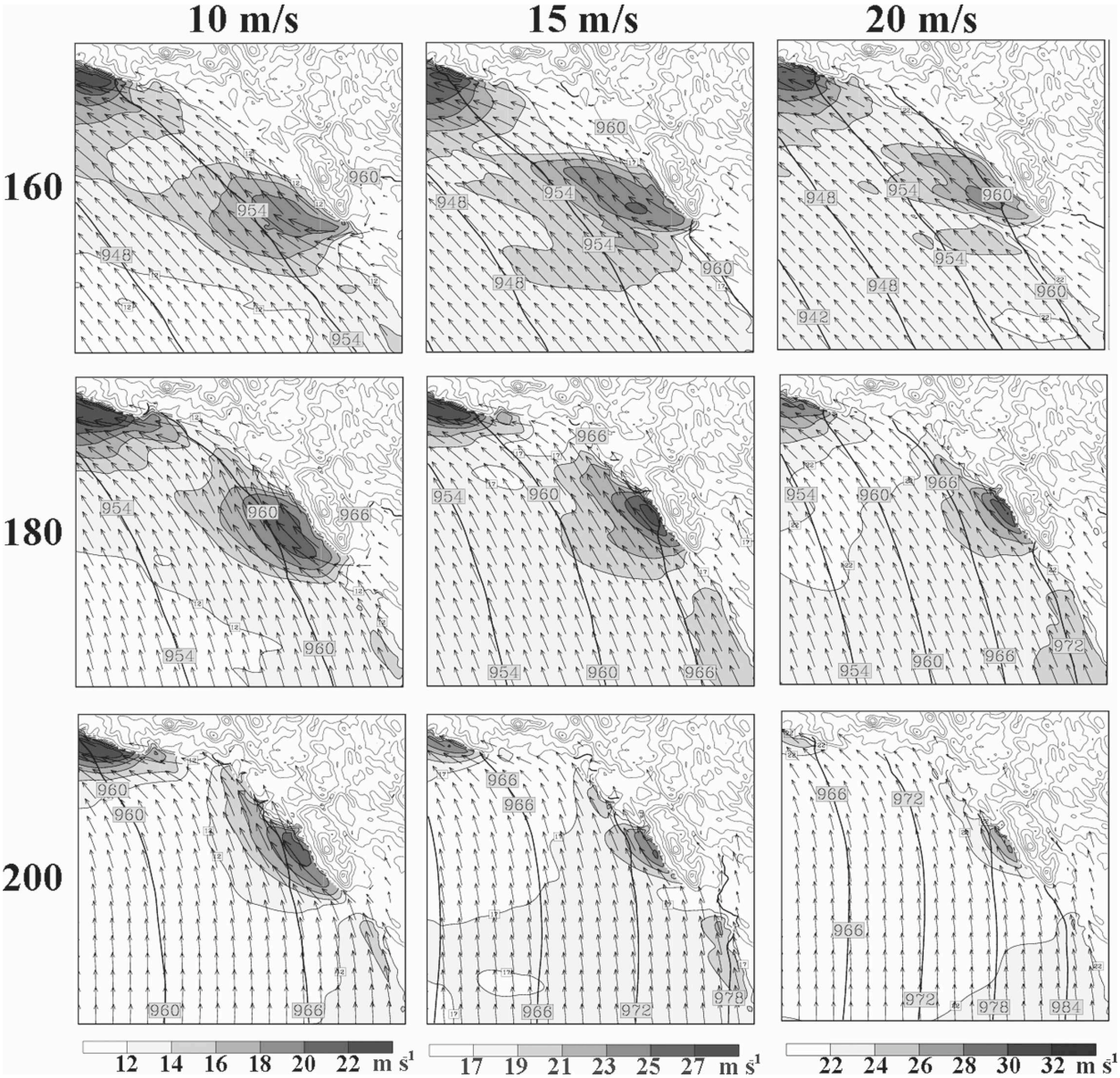

FIG. 14. Wind speeds (gray-shaded every 2 m s^{-1}) and pressure (black every 4 mb) at 500 m MSL for the hybrid jet simulations initialized with cold pool $\Delta T = -10°$C as a function of wind speed (columns) and wind direction (rows).

since there is little gap outflow, and the jets appear more classical (cf. Figs. 10a,b).

b. Hybrid jet width

The width of the hybrid jet is negatively correlated with the U_n (measured >2000 km upstream of the coast) (−0.77) and the wind direction (obtained within the upstream box U) (−0.78) (Table 3). Also, the lines of constant jet width are oriented nearly vertical for increasing U_n and wind direction versus static stability (Figs. 16a,b), which suggests that U_n and wind direction are important in determining the jet width. This is evident in Fig. 17 (top row), where simulations initialized with a wind direction of 160° ($U_n < 5$ m s^{-1}) have wide jets and jet maxima located offshore. In contrast, simulations with wind directions of ≥180° ($U_n \geq 10$ m s^{-1}) (Fig. 17, bottom two rows) have their jet maxima located closer to the coast, since a large U_n favors more downstream advection of mountain-induced perturbation as well as downward mixing of onshore-directed momentum as shown in OL07. Therefore, wind direction is the most important factor in governing the occurrence of the gap outflows, which in turn have a profound impact on the total offshore extent of the hybrid jet.

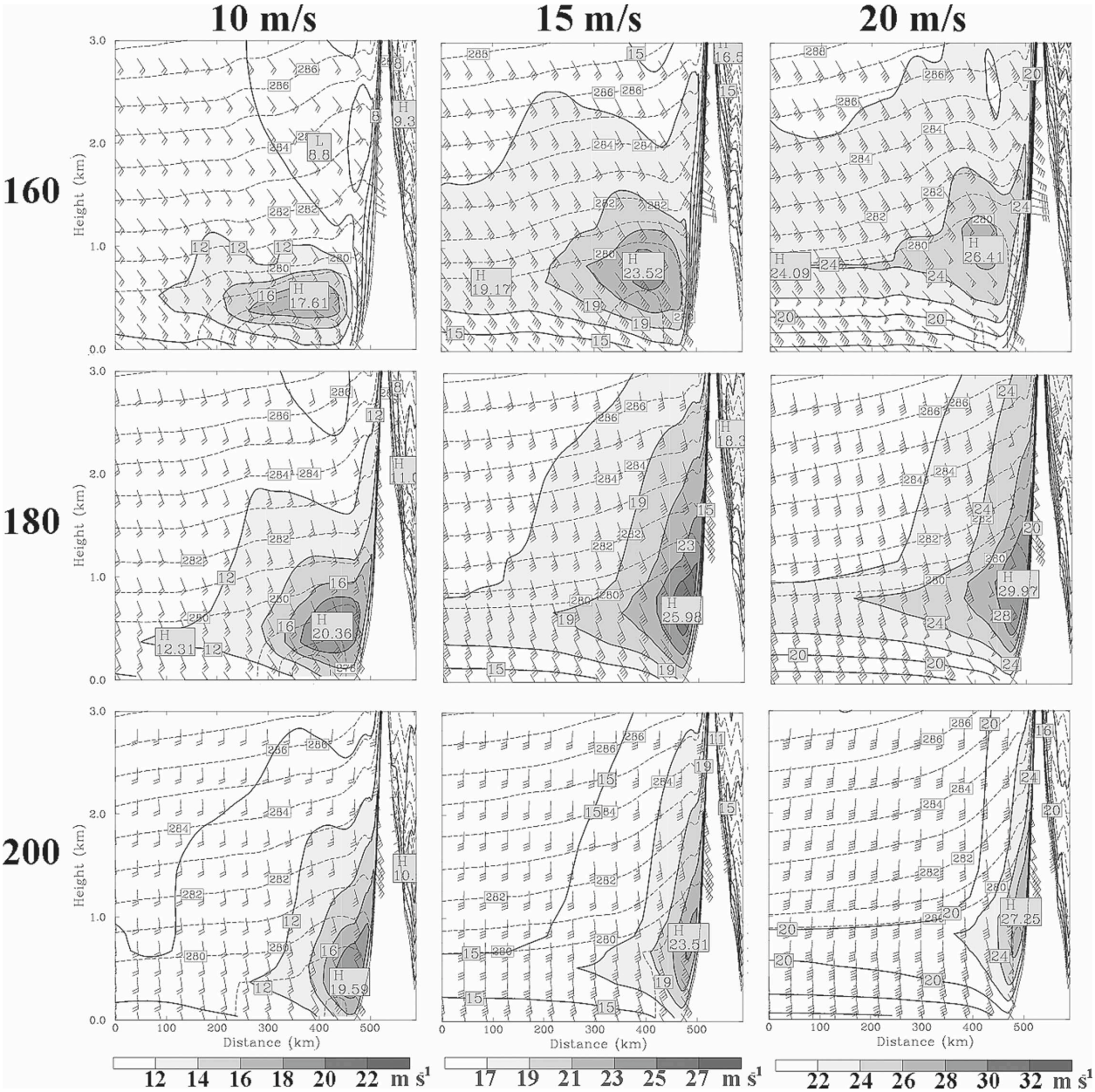

FIG. 15. Cross sections of wind speed (gray-shaded every 2 m s^{-1}), wind barbs (full barb = 10 kt), and potential temperature (dashed gray every 1 K) taken across A–A′ for the hybrid jet simulations initialized with cold pool $\Delta T = -10°$C as a function of wind speed (columns) and wind direction (rows).

The strength of the inland cold pool is a secondary factor in the barrier jet width, which only made a strong impact for the nearly coast-parallel wind directions. Figures 17 and 18 show the impact of cold pool strength versus wind direction for the same ambient wind speed (15 m s^{-1}), where the offshore extent is primarily a function of wind direction for all cases with wind directions of ≥180° (bottom two rows). However, for flows oriented at 160°, the inland cold pool is effectively accelerated through the mountain gap, initiating gap outflow. This leads to an approximate doubling of the jet width for a cold pool approaching −15°C. In contrast, a pressure gradient orientated more coast-parallel does not favor acceleration of the cold pool through the coastal gaps. This is consistent with the results of Zängl (2005), in which Alpine cold pool drainage was found to be highly sensitive to the ambient wind direction.

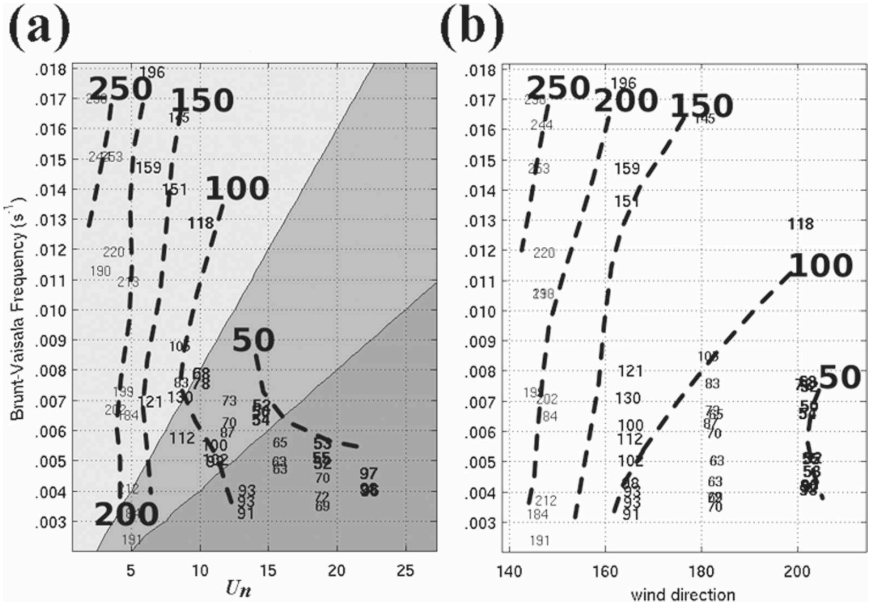

FIG. 16. Total offshore extent (numbers and dashed every 25 km) for the hybrid jets as a function of N and (a) U_n and (b) wind direction. The variations in the size and thickness of the numbers are relative to the initialized wind direction (see Fig. 8).

c. *Hybrid jet height*

The range of hybrid jet heights (250–950 m MSL) is comparable to the heights measured in the classical barrier jet simulations (Figs. 11 and 19). A strong correlation (0.81) exists between jet height and the wind speed (measured within box U). Since all hybrid simulations were initialized with $N = 0.01\ \mathrm{s}^{-1}$, correlations with static stability were not meaningful.

The wind speed impact on the hybrid jet height can be seen in Fig. 15, where simulations with the largest wind speeds have the highest barrier jets (right column). These same conditions also dictated the jet heights in the classical jet simulations. During conditions of strong gap outflow, the jet maximum is located at the top of the gap outflow (upper left-hand corner of Fig. 15 and the adjacent panels), but when gap outflow is not initiated or mixed away by the strong ambient winds, the hybrid jet height is controlled by the same mechanisms as the classical jets (noted in section 5).

7. Discussion and conclusions

Three-dimensional idealized simulations with the MM5 were completed down to 6-km grid spacing over the southeast Alaskan coast. The model was initialized with varying wind speeds, wind directions, and static stabilities for a set of classical barrier jet simulations, while an inland cold pool was initialized for the hybrid jet simulations.

The broad inland plateau rotates the upstream winds cyclonically to become more terrain-parallel 500–1000 km upstream of the coast. Simulations without the broad inland terrain resulted in a weaker and narrower coastal barrier jet. The large-scale mountain anticyclone produced by a broad plateau acts to "precondition" the impinging flow for barrier jet development by turning the far upstream flow to become more barrier-parallel, which increases the likelihood of flow blocking near the coast. The combination of the flow with the mountain anticyclone and near-coast accelerations acts to expand the region of enhanced barrier-parallel wind speeds. This reinforces the results obtained by the two-dimensional simulations of Braun et al. (1999a), which showed that barrier jets are stronger for flow over a plateau-like barrier. Our results also show that there is a wind direction dependence on the large-scale mountain anticyclone caused by variations in the width of the downstream (relative to Mt. Fairweather) inland plateau. This resulted in the strongest mountain anticyclones for the most coast-perpendicular wind directions (220°), which contributed ~50% of the total momentum of the barrier jet when compared to a simulation with the inland terrain removed.

Loescher et al. (2006) showed that there was an approximate equal number of hybrid versus classical jets along the southeast Alaskan coast and the maximum wind speeds were comparable, while the hybrid jets have a ~10-km-larger median jet width. They also

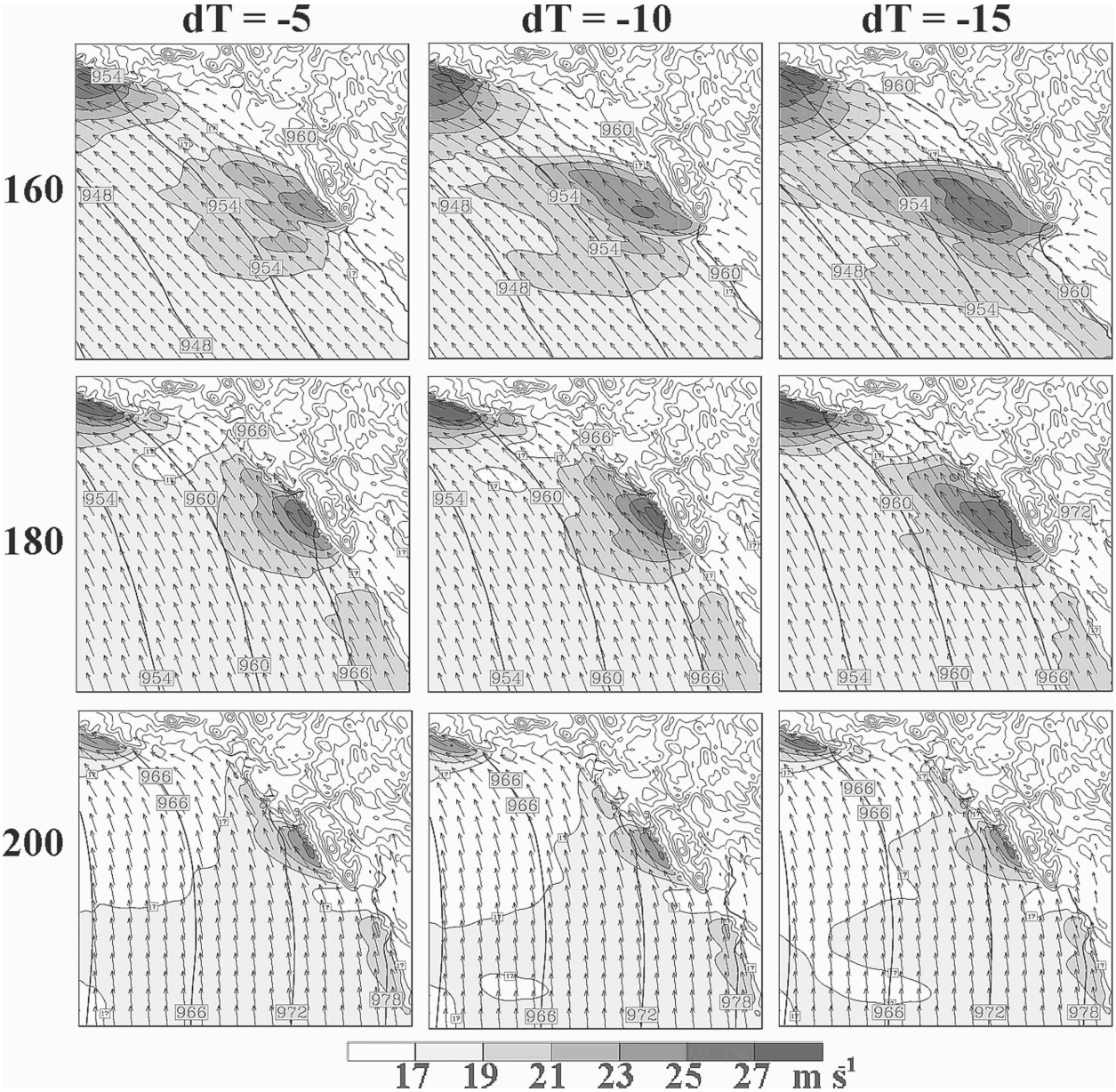

FIG. 17. Wind speed (gray-shaded every 2 m s^{-1}) and pressure (black every 4 mb) at 500 m MSL for the hybrid jet simulations initialized with a constant wind speed of 15 m s^{-1} and $N = 0.01$ s^{-1} as a function of cold pool strength (°C; columns) and wind direction (°; rows).

found tail in the jet width distribution to ~250 km. The simulations presented herein also show slightly wider jets for the hybrid jets and suggest that the long (~250 km) tail in the distribution of jet widths in Loescher et al. (2006) is favored for ambient winds oriented nearly terrain-parallel (~160°) and strong static stability ($N >$ 0.01 s^{-1}). Although the largest mountain anticyclones were found in the most terrain-perpendicular ambient wind directions (220°), the larger terrain-parallel wind speed perturbations decayed by a factor of e more rapidly than the weaker terrain-parallel wind speed perturbations associated with the more terrain-parallel ambient flows (160°).

When the low-level ambient flow was nearly coast-parallel with an inland cold pool, offshore-directed gap outflows are initiated. This increases the offshore extent of the hybrid jets during periods of strong gap outflows, but it has little effect after the inland cold pool is drained or when the gap outflow was effectively mixed away in conditions of strong ambient wind

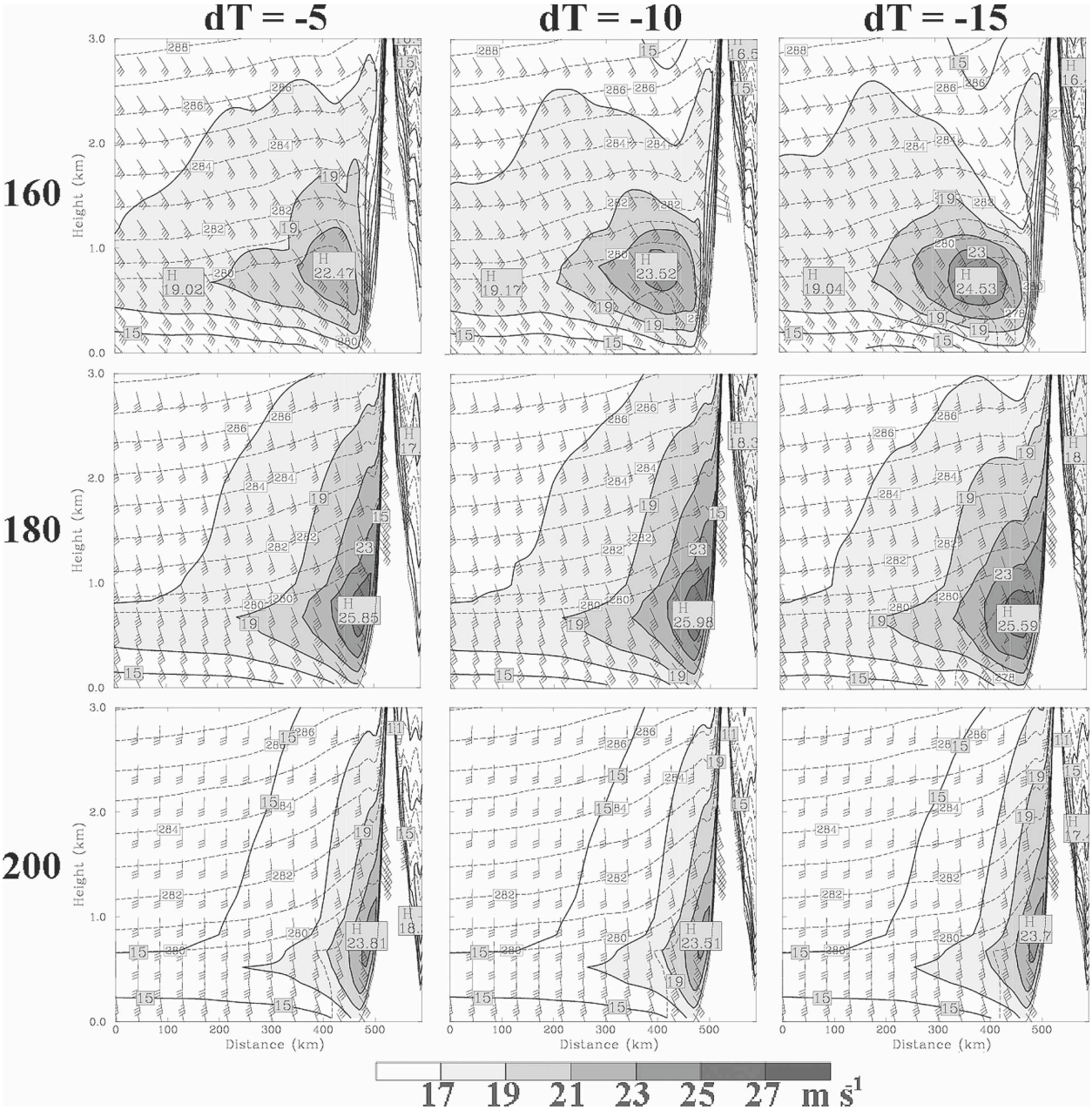

FIG. 18. Cross sections of wind speed (gray-shaded every 2 m s^{-1}) and potential temperature (dashed gray every 1 K) taken across A–A′ for the hybrid jet simulations initialized with a constant wind speed of 15 m s^{-1} and N = 0.01 s^{-1} as a function of cold pool strength (°C; columns) and wind direction (°; rows).

speed. The gap outflows also act to shift the position of the jet maximum farther away from the coast. In contrast, flows oriented more perpendicular to the coast (having a pressure gradient oriented more coast-parallel) prevent acceleration of the cold pool through the coastal gaps. Thus, the hybrid barrier jet structures forced by southwesterly flows resembled the classical barrier simulations, which have no inland cold pool initialized.

Our largest simulated wind speed enhancements for classical jets (~1.9) occurred for a low Fr (~0.3–0.4), which is consistent with other studies (Ólafsson and Bougeault 1996; Braun et al. 1999a; Petersen et al. 2003). Low ambient wind speeds (10–15 m s^{-1}) and southerly (170°–180°) wind directions (~30°–45° from coast-parallel) generate the largest wind speed enhancements. The lower momentum flow can more easily become blocked, deflected, and subsequently accel-

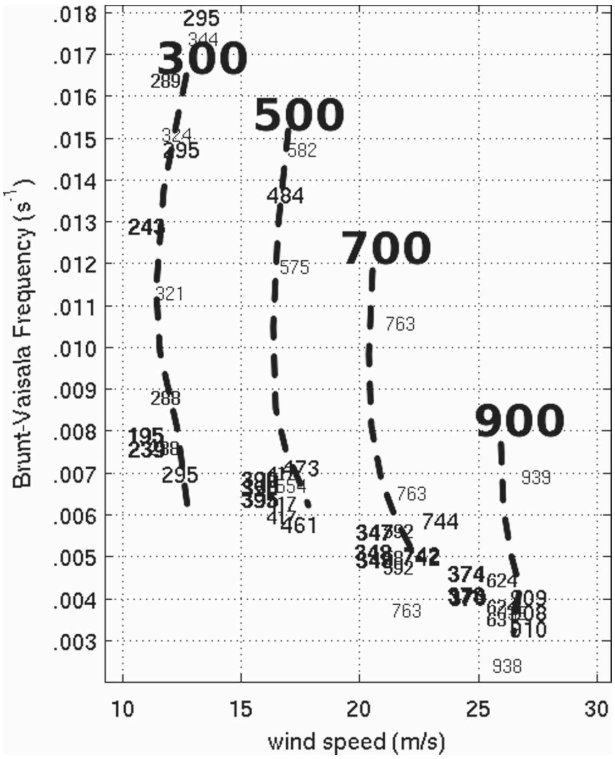

FIG. 19. Hybrid barrier jet height (m) as a function of Brunt–Väisälä frequency (s^{-1}) and wind speed ($m\ s^{-1}$). The variations in the size and thickness of the numbers are relative to the initialized wind direction (see Fig. 8).

erated in a terrain-parallel direction for quasi-two-dimensional terrain. The optimal wind direction for wind speed enhancement is ~175°, because flows oriented more normal to the coast (at 200°–230°) have the largest terrain-parallel accelerations, but also have the largest U_n. On the other hand, flows oriented more parallel to the coast (130°–160°) have a small U_n, but receive little or no acceleration down the along-mountain pressure gradient. Intermediate wind directions (160°–200°) can result in barrier jets produced by a superposition of blocked flow accelerating down the along-barrier pressure gradient as well as contributions from the mountain anticyclone. The influence of the gap outflows is to enhance the coastal jets for the most coast-parallel flows (~160°), shifting the maximum wind speed enhancements to Fr < 0.2 for the hybrid jet simulations.

During periods of maximum gap outflow (hours 6–18), the height of the jet maximum is typically at the top of the shallow gap outflow (~500 m MSL) and typically lower than the jet maximum in the classical jet simulations. After the gap outflows begin to weaken (~18 h), the hybrid jet heights are comparable to the classical jet heights. At this time, the jet height (both classical and hybrid) is positively correlated with total wind speed, U_{total}, while it is negatively correlated with static stability, N, suggesting that the height of the jet maximum approximately scales as U_{total}/N. The total wind speed, U_{total}, governs the strength of the turbulent mixing in the PBL by increasing the frictionally induced wind shear, but this mixing is countered by increases in static stability. The turbulent mixing enhances the stability at the top of the PBL, thus modulating the height of the barrier jets.

This numerical study advances our understanding of the nature of barrier jets produced by the interaction of impinging flow toward the complex three-dimensional orography of coastal Alaska. Additional insight may be gained by including time-dependent barrier jet structures within landfalling idealized baroclinic waves as well as some other physical processes (moisture, surface fluxes, radiation, etc.).

Acknowledgments. The authors thank Dr. Scott Braun of NASA Goddard Space Flight Center, Dr. Nicholas Bond of the NOAA/Pacific Marine Environment Laboratory, and Dr. John Brown of NOAA/Earth System Research Laboratory for their comments and suggestions on improving this manuscript. This research was supported by the National Science Foundation (ATM-0240402). Use of the MM5 was made possible by the Microscale and Mesoscale Meteorological (MMM) Division of the National Center for Atmospheric Research (NCAR), which is supported by the National Science Foundation.

REFERENCES

Bannon, P. R., 1986: Deep and shallow quasigeostrophic flow over mountains. *Tellus,* **38A,** 162–169.

——, and P. C. Chu, 1988: Anelastic semigeostrophic flow over a mountain ridge. *J. Atmos. Sci.,* **45,** 1020–1029.

Barstad, I., and S. Grønås, 2005: Southwesterly flows over southern Norway—Mesoscale sensitivity to large-scale wind direction and speed. *Tellus,* **57A,** 136–152.

Bond, N. A., and R. G. Fleagle, 1988: Prefrontal and postfrontal boundary layer processes over the ocean. *Mon. Wea. Rev.,* **116,** 1257–1273.

——, and B. A. Walter, 2002: Research aircraft observations of the mean and turbulent structure of a low-level jet accompanying a strong storm. *J. Appl. Meteor.,* **41,** 1210–1224.

Braun, S. A., R. A. Houze, and B. F. Smull, 1997: Airborne dual-doppler observations of an intense frontal system approaching the Pacific Northwest coast. *Mon. Wea. Rev.,* **125,** 3131–3156.

——, R. Rotunno, and J. B. Klemp, 1999a: Effects of coastal orography on landfalling cold fronts. Part I: Dry, inviscid dynamics. *J. Atmos. Sci.,* **56,** 517–533.

——, ——, and ——, 1999b: Effects of coastal orography on landfalling cold fronts. Part II: Effects of surface friction. *J. Atmos. Sci.,* **56,** 3366–3384.

Buzzi, A., and S. Tibaldi, 1977: Inertial and frictional effects on rotating and stratified flow over topography. *Quart. J. Roy. Meteor. Soc.,* **103,** 135–150.

Colle, B. A., and C. F. Mass, 1996: An observational and modeling study of the interaction of low-level southwesterly flow with the Olympic Mountains during COAST IOP 4. *Mon. Wea. Rev.,* **124,** 2152–2175.

——, B. F. Smull, and M.-J. Yang, 2002: Numerical simulations of a landfalling cold front observed during COAST: Rapid evolution and responsible mechanisms. *Mon. Wea. Rev.,* **130,** 1945–1966.

——, K. A. Loescher, G. S. Young, and N. S. Winstead, 2006: Climatology of barrier jets along the Alaskan Coast. Part II: Large-scale and sounding composites. *Mon. Wea. Rev.,* **134,** 454–477.

Cui, Z., M. Tjernström, and B. Grisogono, 1998: Idealized simulations of atmospheric coastal flow along the central coast of California. *J. Appl. Meteor.,* **37,** 1332–1363.

Delsol, F., K. Miyakoda, and R. H. Clarke, 1971: Parameterized processes in the surface boundary layer of an atmospheric circulation model. *Quart. J. Roy. Meteor. Soc.,* **97,** 181–208.

Grell, G. A., J. Dudhia, and D. R. Stauffer, 1995: A description of the fifth-generation Penn State/NCAR Mesoscale Model (MM5). NCAR Tech. Note NCAR/TN-398+STR, 138 pp.

Klemp, J. B., and D. R. Durran, 1983: An upper boundary condition permitting internal gravity wave radiation in numerical mesoscale models. *Mon. Wea. Rev.,* **111,** 430–444.

Lackmann, G. M., and J. Overland, 1989: Atmospheric structure and momentum balance during a gap-wind event in Shelikof Strait, Alaska. *Mon. Wea. Rev.,* **117,** 1817–1833.

Loescher, K. A., G. S. Young, B. A. Colle, and N. S. Winstead, 2006: Climatology of barrier jets along the Alaskan Coast. Part I: Spatial and temporal distributions. *Mon. Wea. Rev.,* **134,** 437–453.

Macklin, S. A., N. A. Bond, and J. P. Walker, 1990: Structure of a low-level jet over lower Cook Inlet, Alaska. *Mon. Wea. Rev.,* **118,** 2568–2578.

Ólafsson, H., and P. Bougeault, 1996: Nonlinear flow past an elliptic mountain ridge. *J. Atmos. Sci.,* **53,** 2465–2489.

Olson, J. B., 2007: The structure and dynamics of barrier jets along the southeast Alaskan Coast. Ph.D. thesis, Stony Brook University, 156 pp.

——, and B. A. Colle, 2007: A modified approach to initialize an idealized extratropical cyclone within a mesoscale model. *Mon. Wea. Rev.,* **135,** 1614–1624.

——, ——, N. A. Bond, and N. Winstead, 2007: A comparison of two coastal barrier jet events along the southeast Alaskan coast during the SARJET field experiment. *Mon. Wea. Rev.,* **135,** 3642–3663.

Orr, A., J. Hunt, R. Capon, J. Sommeria, D. Cresswell, and A. Owinoh, 2005: Coriolis effects on wind jets and cloudiness along coasts. *Weather,* **60,** 292–299.

Overland, J. E., and N. A. Bond, 1993: The influence of coastal orography: The Yakutat storm. *Mon. Wea. Rev.,* **121,** 1388–1397.

——, and ——, 1995: Observations and scale analysis of coastal wind jets. *Mon. Wea. Rev.,* **123,** 2934–2941.

Parish, T. R., 1982: Barrier winds along the Sierra Nevada Mountains. *J. Appl. Meteor.,* **21,** 925–930.

Peng, M. S., J. H. Powell, R. T. Williams, and B.-F. Jeng, 2001: Boundary layer effects on fronts over topography. *J. Atmos. Sci.,* **58,** 2222–2239.

Petersen, G. N., J. E. Kristjánsson, and H. Ólafsson, 2003: The effect of upstream wind direction on atmospheric flow in the vicinity of a large mountain. *Quart. J. Roy. Meteor. Soc.,* **131,** 1113–1128.

Pierrehumbert, R., 1984: Linear results on the barrier effects of mesoscale mountains. *J. Atmos. Sci.,* **41,** 1356–1367.

——, and B. Wyman, 1985: Upstream effects of mesoscale mountains. *J. Atmos. Sci.,* **42,** 977–1003.

Schwerdtfeger, W., 1974: Mountain barrier effect on the flow of stable air north of the Brooks Range. *Proc. 24th Alaskan Science Conf.,* Fairbanks, AK, Geophysical Institute, University of Alaska Fairbanks, 204–208.

Smedman, A. S., H. Bergström, and U. Högström, 1995: Spectra, variances and length scales in a marine boundary layer dominated by a low level jet. *Bound.-Layer Meteor.,* **76,** 211–232.

Smith, R. B., 1979a: The influence of mountains on the atmosphere. *Advances in Geophysics,* Vol. 21, Academic Press, 87–230.

——, 1979b: Some aspects of quasi-geostrophic flow over mountains. *J. Atmos. Sci.,* **36,** 2385–2393.

Smolarkiewicz, P. K., and R. Rotunno, 1989: Low Froude number flow past three-dimensional obstacles. Part I: Baroclinically generated lee vortices. *J. Atmos. Sci.,* **46,** 1154–1164.

Winstead, N., and Coauthors, 2006: Using SAR remote sensing, field observations, and models to better understand coastal flows in the Gulf of Alaska. *Bull. Amer. Meteor. Soc.,* **87,** 787–800.

Yeh, H.-C., and Y.-L. Chen, 2003: Numerical simulations of the barrier jet over northwestern Taiwan during the mei-yu season. *Mon. Wea. Rev.,* **131,** 1396–1407.

Zängl, G., 2002: An improved method for computing horizontal diffusion in a sigma-coordinate model and its application to simulations over mountainous topography. *Mon. Wea. Rev.,* **130,** 1423–1432.

——, 2003: The impact of upstream blocking, drainage flow, and the geostrophic pressure gradient on the persistence of cold-air pools. *Quart. J. Roy. Meteor. Soc.,* **129,** 117–137.

——, 2005: Formation of extreme cold-air pools in elevated sinkholes: An idealized numerical process study. *Mon. Wea. Rev.,* **133,** 925–941.

Zhang, D., and R. Anthes, 1982: A high-resolution model of the planetary boundary layer—Sensitivity tests and comparisons with SESAME-79 data. *J. Appl. Meteor.,* **21,** 1594–1609.